Migration of a single particle suspended in non-Newtonian fluid

Teresa Tuccillo

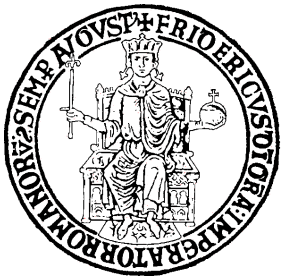

Scientific Commettee

Prof. Pier Luca Maffettone

Dr. Francesco Greco

Prof. Nino Grizzuti

Contents

1 Introduction

Solid-liquid dispersions, also known as suspensions, are widely used in industry. Suspensions are used in paints, dyestuffs, inks, cosmetics, detergents, and pharmaceuticals. Since the original work of Einstein[1] one hundred years ago on the effective viscosity of a dilute suspension of rigid spheres many studies have been devoted to determining theoretically or by experiments the "effective" properties, e.g. viscosity, sedimentation rate, diffusion coefficients, etc., of suspensions under a wide range of conditions. Indeed the suspension is often non-Newtonian and the particles can cause an alteration of the overall rheological properties. Particles in suspension may interact through both hydrodynamic and nonhydrodynamic forces, where the latter may be any type of colloidal, interparticle or external force. In particular the motion of particles immersed in a liquid subjected to flow is important in several applications such as surface cleaning, deposition of particles in filtration, mobilization in porous media, etc. Indeed, such a problem has been studied for many decades and consequently, a very ample literature does exist on suspension mechanics, often centered on specific topics (see e.g. the reviews [2],[3],[4]). Most of the previous works focused on the motion in a Newtonian fluid. In the last years the viscoelasticity of the suspending fluid has also been taken into account, as the motion of the particles depends on the rheological properties of the suspending fluid. In this work we analyze the migration of an isolated particle in shear flow by means of a finite element code. The simulations are performed by considering a viscoelastic suspending fluid, by neglecting inertia. In particular we will analyze the motion of a single rigid, non-Brownian, inertialess, circular particle (2D problem) moving in a channel filled by a viscoelastic fluid under shear flow in a rectangular domain. First we will show that the particle moves towards a wall if immersed in a non-Newtonian fluid under continuous shear flow, in qualitative agreement with experimental findings. Anyway most of the experiments are performed under oscillatory shear flow, so we will study the effect of oscillation on the migration of the particle and we will compare our results with experimental data. Finally we will report results of migration when particle is moving between two concentric rotating cylinders. We will show that the migration is strongly affected by the curvature of the two cylinders. We will also show the effect of the

suspending fluid and the particle size.

In all our simulations the suspending fluid used is a Giesekus fluid, i.e. a shear thinning fluid in which both the normal stresses difference exist. An ALE particle mover is combined with a DEVSS/SUPG formulation with a log-representation of the conformation tensor giving stable and convergent results up to high Deborah numbers. To optimize the computational effort and reduce the remeshing and projection steps, needed as soon as the mesh becomes too distorted, a backprojection of the flow fields is performed. As a result, the particle is allowed to move along the cross-streamline direction only and the mesh distortion is drastically reduced.

2 State of the art

The problem of an isolated particle motion in a flow has a significant importance in several applications such as surface cleaning, deposition of particles in filtrations, mobilization in porous media, etc. Indeed such a problem has been studied for many decades. However, most of the previous works focused their analysis on the motion in a Newtonian fluid. Recently, due to the relevance in many application fields, the viscoelasticity of the suspending fluid is taken into account, in fact the motion of the particle depends on the rheological problem of the suspending fluid. Is well known that a non-Newtonian fluid displays a complex behavior under shear flow, for example shear-thinning viscosity, normal stresses difference, and so on. The addition of particles to these fluids further complicates their behavior by changing the rheological properties (see Fig 2 ,[5])and the flow field as showed in Figure 1([6],[7]).

In this Chapter we report an analysis of previous work about the motion of particles in Newtonian and non-Newtonian fluids. Our aim is to understand the principal phenomena that appear under flows.

In celebrated experiments, Segré and Silberberg (1961)([8],[9])discovered that neutrally buoyant spherical particles in a pipe flow of a Newtonian fluid migrate to a radial position of about 0.6 times the tube of channel, in other words they found the existence of an equilibrium height in the channel where the particles tend to migrate. Many analytical theories

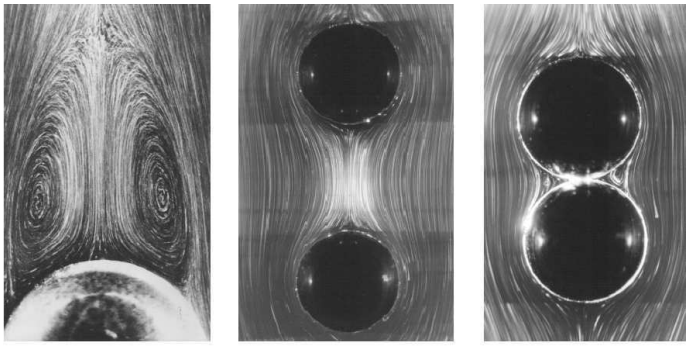

Figure 1: Streamline pattern visualized by suspending aluminum powder. (from [6],[7]).

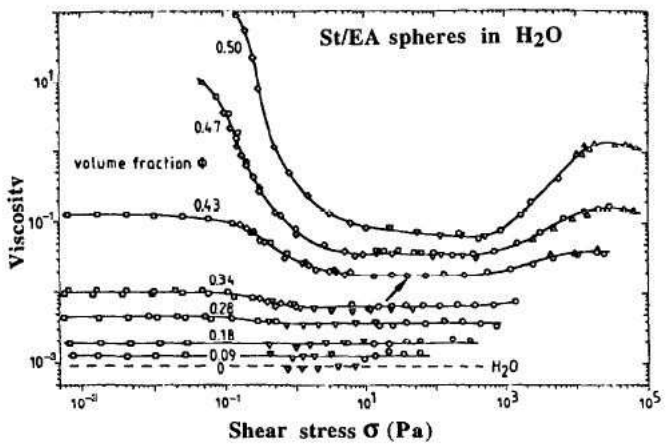

Figure 2: Viscosity versus shear stress for aqueous suspensions of charged poly(styreneethylacrylate) copolymer spheres at various volume fractions. In spite of the Newtonian nature of the suspending fluid, non linear behaviors can be observed.(from [5]).

were also derived in the past, giving expressions for the lift force experienced by a particle in low Reynolds number Newtonian flows and simple geometries. An enlightening paper by [10] gave an expression for the potential lift force on a sphere in an unbounded shear flow. Such a theory was later generalized by [11] and [12] removing some constraints on the flow parameters.

The motion of a sphere in the presence of a flat wall in shear flow was studied by using a perturbative approach by [13], [14] and [15]. They found the critical conditions for Reynolds number to let the sphere separate from the wall.

All the references cited above refer to a Newtonian suspending fluid. The viscoelastic nature of the suspending medium is, however, relevant in many processes (polymer melts with fillers, rubbers, cosmetics, foods, etc.). In this case, few experimental data sets on migration are available.

In 1966 Karnis and Mason [16] studied experimentally the motion of a single rigid particle suspended in a viscoelastic fluid in both Couette and Poiseuille flows without inertial effect. They found that in a tube flow, the particle migrated toward the center of the channel, instead in a Couette flow the particle migration occurred from the center toward the

outer cylinder. In the latter case the direction of the motion was independent of the sense of rotation and whether the inner or outer cylinder was rotating. Moreover they found that the rate of migration increased with increasing the particle diameter. As a viscoelastic fluid they used a solution of polyacrylamide in water, which exhibited significant shear-thinning and elasticity, but they did not report normal stress differences. A few years later, Gauthier et al.(1971)[17] showed that migration occurred in the opposite direction if the particle was suspended in a purely viscous fluid, i.e. in a fluid which shows a strong shear thinning, but very weak normal stresses. However the rheological data of these experiments are incomplete. Particle migration is also observed under torsional shear. In particular Karis et al[18, 19] reported results on migration in torsional flow between two flat plates. For slow rotation rates they observed inwards migrations, instead for higher rotation rates the migrations was in the opposite directions. The unexpected results of their work was the existence of a critical radial distance: when placed closer to the center than the critical radius, the particle drifted to the center, with the opposite behavior for initial positions beyond the critical radius. In 1985, Prieve and coworkers,[20], studied influence of particle radius of the migration of a rigid sphere under torsional flow. They found that the migration velocity increases with the particle dimensions. Feng and Joseph [21] performed similar experiments, but with a viscoelastic, shear-thinning fluid. They did not find the presence of a critical radius in fact they observed migrations only in the outward direction and found that radial velocities of migrating particles were constant over the distance traveled by the particle.

Migration also occurs in concentrated systems. In 1977 Michele et al.,[22], first reported very interesting results on the chaining and aggregation of spherical particles in a viscoelastic fluid. They subjected suspensions composed of monodisperse glass spheres ($60 - 70$ mm) in either polyacrylamide or polyisobutylene solutions at concentrations ranging from 2% to 10% (by weight) to a oscillatory rectilinear shear flow between two glass slides and they found that the particles formed long string-like structures oriented in the flow direction. The formation of these structures occurs after a migration of particles. Jefri and Zahed (1988)[23] reported results for cross-flow migration of solid spherical nylon balls (0.238 cm diameter and volume fraction equal to 0.02) in three

different mediums carried out under plane- Poiseuille flow conditions in a perspex slit channel. The three different fluids employed for suspensions are a Newtonian medium, a nonshear-thinning elastic medium and a shear thinning elastic medium. In the Newtonian medium, particle distribution was found to be uniform, whereas in a nonshear-thinning medium, migration tended toward the center line resulting in formation of a narrow core. In the viscoelastic shear-thinning medium, the solid particles concentration is observed between two altitudes measured at about 0.35 cm from top and bottom sides of the slit channel and at about 0.6 cm from the central axis of the channel and, in these conditions, they observed the formation of a chain structure. Tehrani (1996)[24] reported that particles migrate to the core region in tube flow of a viscoelastic suspension. It was found that particle migration in such fluids is controlled by the elastic properties of the suspending fluid and the shear rate gradient. In fluids with low but measurable normal stresses and dominant shear-thinning properties, particles migrate to regions of lower shear rate.Shear-induced migrations, observed in shear flows of concentrated monodisperse suspensions, can be explained by inclusion of shear-induced normal stresses in the rheological model, as stated by Morris and Bulay in 1999[25]. They used a simple model for the normal stresses to explain the anomalous migration observed in experiments on parallel-plate and cone-plate devices. Particle migration was also observed by Ponche and Dupuis (2005)[26] in a suspension of glass spheres in a viscoelastic polymer solution submitted to shear flows in a plate and cone geometry. After shearing, the beads located themselves on concentric rings. In each ring they regroup in small packs. The suspending medium is a 3% high molecular weight poly-iso-butylene (PIB) solution in decalin, a shear thinning, elastic fluid. The fluid is filled with glass spherical beads at a volume fraction of 5%. Their diameter ranges from 38 to 53 mm. After shearing they observed a depletion region in the central zone of the pattern in each case, well defined concentric rings containing most of the solid particles and, in each ring, regular spaced small packs of particles. The migration of beads is due to particle-particle interaction. Thin interaction is a very complicated process governed by various factors (Lee et al. 2002): in Newtonian fluid, in addition to the viscous forces, fluid inertia and unsteadiness play important roles when the particle loading is high and the shear rate is large. In polymer solutions, viscoelasticity,

shear thinning and normal stress differences affect the particle-particle interaction together with the possibility of apparent wall-slip due to the migration and concomitant depletion of polymer molecules from the gap. All these works showed that in non-Newtonian fluids migrations and aggregations of particles occur. These two phenomena are strictly related: in fact thee migration is the first step for the alignment and, then, for the chaining of particles.

On the theoretical side, and limiting to simple shear only, which is the case of interest in our paper, we are aware of only two works explicitly addressing the viscoelasticity-induced cross-flow migration, but at vanishing flow rates [27,] or at modest flow rates in a 2D approximation [28,]. In 1976 Ho and Leal [27] demonstrated that in a second order fluid, the presence of normal stresses caused the migration of the particle in the direction of decreasing absolute shear rate, i.e. toward the center-line in a Poiseuille flow and toward the outer cylinder in a Couette flow. In their numerical simulations, Huang et al. [28] reported the results of direct numerical simulation of the motion of a two-dimensional circular cylinder in Couette flow and in Poiseuille flow of an Oldroyd-B fluid. The migration is affected by the inertia, elasticity, the blockage ratio and shear thinning. They found that the particle migrates toward the wall in both Couette and Poiseuille flow in presence of inertia. Instead, in absence of inertia, in Couette flow particles migrate toward the nearby wall and the rate of migration increases with increasing the shear thinning of the suspending fluid. They also examined the effect of blockage ratio, i.e. the ratio between the diameter of the particle and the width of the domain. They found that a particle moves closer to the wall as the width of the channel becomes smaller. They also studied the influence on particle lift of fluid parameters, particle size/channel height ratio. [28] accounted for shear thinning with an ad-hoc modification of the Oldroyd-B model. Thus, such a viscoelastic constitutive equation is rather unrealistic, with rheological properties rarely found in real viscoelastic fluids (constant first normal stress coefficients, no second normal stresses, divergent elongational viscosity). The main conclusion of [27] and [28] is that migration (if present) has to be ascribed to the presence of normal stresses.

Only recently, a careful and complete analysis by Lormand and Phillips [29] reported on the migration of a sphere in a viscoelastic fluid in a Couette apparatus with small curvature. Their data clearly show the

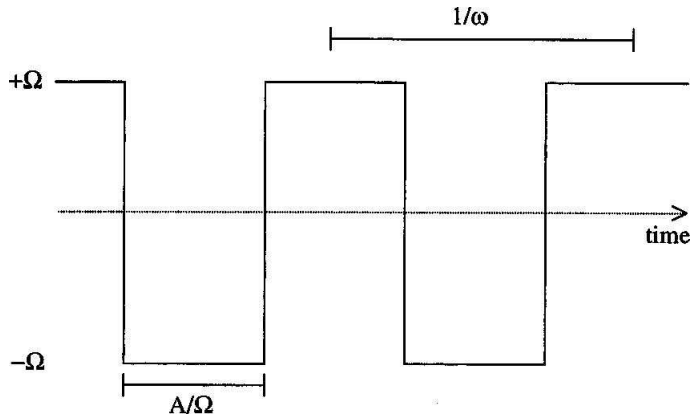

Figure 3: Oscillatory velocity pattern applied to the inner cylinder in Lormand and Phillips experimente (from [29]). Ω is the angular velocity of the rotating cylinder.

tendency of the particle to migrate towards the walls of the flow cell. We focused our attention on their work in order to compare our results with their experimental data. Particle migration experiments are performed in a concentric cylinder apparatus undergoing time-dependent oscillations of the inner cylinder. For their experiments the authors used polystyrene spheres (diameters of 300-600 μm) in a 13% solution of PIB in TD, which is a shear-thinning solution. The experiments were performed by inserting a particle into the annulus at a certain distance from the walls and oscillating the inner cylinder. The applied velocity was a square wave, as shown in figure 3.

They defined the amplitude A as the angular distance traveled by the inner cylinder before changing direction; the frequency f as the inverse of the period of the oscillation and the angular velocity Ω

$$\Omega = 2Af \tag{1}$$

Their experiments were carried out varying, one at a time, initial position, frequency, amplitude, and particle size. As we will show in Chapter 6 our simulations and their experimental results are in a perfect qualitative agreement.

3 Governing equations

We consider a single, rigid, non-Brownian, inertialess, circular particle (2D problem) moving in a channel filled by a viscoelastic fluid. The problem is schematized in Figure 4: a particle with diameter $D_p = 2R_p$, denoted by $P(t)$ and boundary $\partial P(t)$, moves in a rectangular domain, W, with dimensions L and H along $x-$ and $y-$axis respectively and external boundaries denoted by Γ_i $(i = 1 \dots 4)$. The Cartesian x and y coordinates are selected with the origin at the center of the domain. On the upper and lower boundaries, equal and opposite velocities are imposed that, for an unfilled fluid,would generate the shear flow depicted on the right part of the same figure.

The vector $\boldsymbol{x}_p = (x_p, y_p)$ gives the position of the center of the particle P. In order to evaluate particle rotation, an angular information, $\boldsymbol{\Theta} = \Theta \boldsymbol{k}$, is also associated with the particle, where $\boldsymbol{k}$ is the unit vector in the direction normal to the $x - y$ plane. The particle moves according to the imposed flow and its rigid-body motion is completely defined by the translational velocity, denoted by $\boldsymbol{U}_p = d\boldsymbol{x}_p/dt = (U_p, V_p)$ and angular velocity, $\boldsymbol{\omega} = d\boldsymbol{\Theta}/dt = \omega \boldsymbol{k}$.

The governing equations for the fluid domain, $W - P(t)$, neglecting

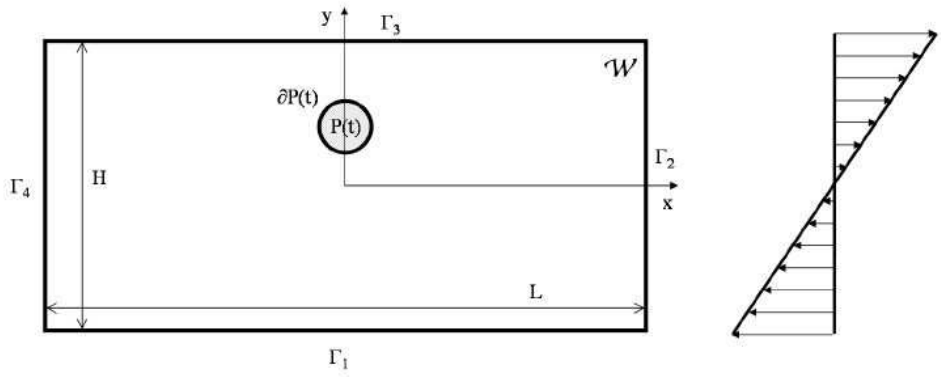

Figure 4: Schematic representation of the problem: a rectangular fluid domain (W) with dimensions L x H with a single particle $P(t)$ is considered. The origin of a Cartesian frame is located at the domain center.

inertia, can be stated as follows:

$$\nabla \cdot \boldsymbol{\sigma} = \mathbf{0} \tag{2}$$

$$\nabla \cdot \boldsymbol{u} = 0 \tag{3}$$

$$\boldsymbol{\sigma} = -p\boldsymbol{I} + 2\eta_s \boldsymbol{D} + \boldsymbol{\tau}_p \tag{4}$$

Equations (2)-(4) are the equations for the momentum balance, the mass balance (continuity) and the expression for the total stress, respectively. In these equations $\boldsymbol{u}$, $\boldsymbol{\sigma}$, p, $\boldsymbol{I}$, $\boldsymbol{D}$, η_s, are the velocity vector, the stress tensor, the pressure, the 2x2 unity tensor, the rate-of-deformation tensor and the viscosity of a Newtonian 'solvent', respectively.

The polymer stress, $\boldsymbol{\tau}_p$, is written as (for the constitutive model chosen, see below):

$$\boldsymbol{\tau}_p = \frac{\eta_p}{\lambda}(\boldsymbol{c} - \boldsymbol{I}) \tag{5}$$

where $\boldsymbol{c}$ is the 'conformation tensor', η_p is the polymer viscosity, and λ is the relaxation time.

We will model the viscoelastic fluid with the Giesekus constitutive equation (for $\boldsymbol{c}$):

$$\lambda \overset{\nabla}{\boldsymbol{c}} + \boldsymbol{c} - \boldsymbol{I} + \alpha(\boldsymbol{c} - \boldsymbol{I})^2 = \mathbf{0} \tag{6}$$

where α is the so-called mobility parameter that modulates the shear thinning behavior. The symbol $(\overset{\nabla}{})$ denotes the upper-convected time derivative, defined as:

$$\overset{\nabla}{\boldsymbol{c}} \equiv \frac{\partial \boldsymbol{c}}{\partial t} + \boldsymbol{u} \cdot \nabla \boldsymbol{c} - (\nabla \boldsymbol{u})^T \cdot \boldsymbol{c} - \boldsymbol{c} \cdot \nabla \boldsymbol{u} \tag{7}$$

Notice that the zero-shear-rate viscosity for the total stress tensor $\boldsymbol{\sigma}$ is given by $\eta_0 = \eta_s + \eta_p$.
The boundary and initial conditions are given by:

$$\boldsymbol{u} = \boldsymbol{U}_p + \boldsymbol{\omega} \times (\boldsymbol{x} - \boldsymbol{x}_p) \quad \text{on } \partial P(t) \tag{8}$$

$$u = \dot{\gamma} y, \quad v = 0 \quad \text{on } \Gamma_1 \text{ and } \Gamma_3 \tag{9}$$

$$\boldsymbol{u}(-L/2, y) = \boldsymbol{u}(L/2, y) \quad \forall\ y \in [-H/2, H/2] \tag{10}$$

$$\boldsymbol{\sigma}(-L/2, y) = \boldsymbol{\sigma}(L/2, y) \quad \forall\ y \in [-H/2, H/2] \tag{11}$$

$$\boldsymbol{c}|_{t=0} = \boldsymbol{c}_0 \tag{12}$$

Equations (8)-(9) are the rigid-body motion on the particle boundary and the shear flow conditions on the upper and lower fluid boundaries, with $\dot{\gamma}$ the applied shear rate. Equations (10) and (11) states periodic boundary conditions on Γ_2 and Γ_4. Since inertia is neglected, no initial condition of the velocity and pressure fields is required whereas the initial conformation tensor condition is necessary (Eq. (12)). In our simulations, we use a stress-free state, i.e. $\boldsymbol{c}|_{t=0} = \boldsymbol{I}$, as initial condition over the whole fluid domain. Notice that, by considering periodicity along $x-$direction, no inflow section exists, therefore we do not need to specify the conformation tensor on any boundary.

The equation governing the rigid-body motion (Eq. (8)) adds (for the 2D case) three additional unknowns, namely, the translational and angular velocities of the particle. So, to obtain particle motion, it is necessary to consider the balance equations for drag force and torque, acting on the particle boundary. Under the assumptions of absence of particle inertia, and of no external forces and torques (force- and torque-free particle), such balance equations are given by:

$$\boldsymbol{F} = \int_{\partial P(t)} \boldsymbol{\sigma} \cdot \boldsymbol{n} ds = \boldsymbol{0} \tag{13}$$

$$\boldsymbol{T} = \int_{\partial P(t)} (\boldsymbol{x} - \boldsymbol{x}_p) \times (\boldsymbol{\sigma} \cdot \boldsymbol{n}) ds = \boldsymbol{0} \tag{14}$$

where $\boldsymbol{F} = (F_x, F_y)$ and $\boldsymbol{T} = T\boldsymbol{k}$ are the total force and torque on the particle boundary, respectively, and $\boldsymbol{n}$ is the outwardly directed unit normal vector on ∂P.

The particle position and rotation are updated by integrating the following kinematic equations:

$$\frac{d\boldsymbol{x}_p}{dt} = \boldsymbol{U}_p, \quad \boldsymbol{x}_p|_{t=0} = \boldsymbol{x}_{p,0} \tag{15}$$

$$\frac{d\boldsymbol{\Theta}}{dt} = \boldsymbol{\omega}, \quad \boldsymbol{\Theta}|_{t=0} = \boldsymbol{\Theta}_0 \tag{16}$$

Equation (16) is completely decoupled from the other equations for a circular particle.

The analysis is carried out by making the above equations dimensionless, using $\dot{\gamma}$ as the characteristic time scale and $\eta_p \dot{\gamma}$ as the scale for the stress. Then, the Deborah number, $De = \lambda \dot{\gamma}$, will appear in the equations.

4 Weak form and implementation

4.1 Weak form

The system of equations (2)-(7) with initial and boundary conditions (8)-(12) and the hydrodynamic equations (13)-(14) form a well-posed problem in the unknowns: p, $\boldsymbol{u}$, $\boldsymbol{c}$, $\boldsymbol{U}_p$, $\boldsymbol{\omega}$. At any time-step the problem is solved and the flow fields, and rigid-body unknowns are evaluated. The kinematic equations (15)-(16) are then integrated to update the particle position and rotation.

Such a system is solved by the finite element method. A log-conformation representation for the conformation tensor has been used [30, 31,]. The original equation for the conformation tensor $\boldsymbol{c}$, Eq. (6), is transformed to an equivalent equation for $\boldsymbol{s} = \log(\boldsymbol{c})$:

$$\dot{\boldsymbol{s}} = \frac{\partial \boldsymbol{s}}{\partial t} + \boldsymbol{u} \cdot \nabla \boldsymbol{s} = \boldsymbol{g}(\boldsymbol{\nabla u^T}, \boldsymbol{s}) \tag{17}$$

An expression for the function $\boldsymbol{g}$ for a Giesekus fluid can be found in [31]. Solving the equation for $\boldsymbol{s}$ instead of the equation for $\boldsymbol{c}$ leads to a substantial improvement of stability for high Deborah numbers.

The finite element method requires the weak formulation of the equations to be solved. Such a weak form for the $W - P(t)$ domain can be stated as follows: For $t > 0$, find $\boldsymbol{u} \in U, p \in P, \boldsymbol{s} \in S, \boldsymbol{G} \in G, \boldsymbol{U}_p \in \Re^2, \boldsymbol{\omega} \in \Re, \boldsymbol{\lambda} \in L^2(\partial P(t))$ such that:

$$\begin{aligned}
&\int_W 2\eta_s \boldsymbol{D}(\boldsymbol{v}) : \boldsymbol{D}(\boldsymbol{u})\, dA - \int_W \nabla \cdot \boldsymbol{v}\, p\, dA + \int_W a(\nabla \boldsymbol{v})^T : \nabla \boldsymbol{u}\, dA \\
&- \int_W a(\nabla \boldsymbol{v})^T : \boldsymbol{G}^T\, dA + \int_{\partial P(t)} [\boldsymbol{v} - (\boldsymbol{V} + \boldsymbol{\chi} \times (\boldsymbol{x} - \boldsymbol{x}_p))] \cdot \boldsymbol{\lambda}\, ds = - \int_W \boldsymbol{D}(\boldsymbol{v}) : \boldsymbol{\tau}_p\, dA,
\end{aligned} \tag{18}$$

$$\int_W q\, \nabla \cdot \boldsymbol{u}\, dA = 0, \tag{19}$$

$$\int_W \boldsymbol{H} : \boldsymbol{G}\, dA - \int_W \boldsymbol{H} : (\nabla \boldsymbol{u})^T\, dA = 0, \tag{20}$$

$$\int_W (\boldsymbol{S} + \tau(\boldsymbol{u} - \hat{\boldsymbol{u}}) \cdot \nabla \boldsymbol{S}) : \left(\frac{\partial \boldsymbol{s}}{\partial t} + (\boldsymbol{u} - \hat{\boldsymbol{u}}) \cdot \nabla \boldsymbol{s} - \boldsymbol{g}(\boldsymbol{G}, \boldsymbol{s}) \right) dA = 0, \tag{21}$$

$$\int_{\partial P(t)} \boldsymbol{\mu} \cdot [\boldsymbol{u} - (\boldsymbol{U}_p + \boldsymbol{\omega} \times (\boldsymbol{x} - \boldsymbol{x}_p))]\, ds = 0, \tag{22}$$

$$\boldsymbol{s} = \boldsymbol{s}_0 \quad \text{at } t = 0 \tag{23}$$

for all $\boldsymbol{v} \in U$, $q \in P$, $\boldsymbol{S} \in S$, $\boldsymbol{H} \in G$, $\boldsymbol{V} \in \Re^2$, $\boldsymbol{\chi} \in \Re$ and $\boldsymbol{\mu} \in L^2(\partial P(t))$, where U, P, S, G are suitable functional spaces. In Eq. (21) $\hat{\boldsymbol{u}}$ is the velocity of the mesh nodes (see below for details).

To improve the numerical stability at high Deborah numbers, a DEVSS-G formulation is implemented [32, 33,] for the momentum balance, Eq. (18), and the SUPG technique [34,] is used for the constitutive relation, Eq. (21).

The τ parameter in Eq. (21) is given by $\tau = \beta h/2U_e$, where β is a dimensionless constant, h is a typical size of the element and U_e is a characteristic velocity for the element. In our simulations, we have chosen $\beta = 1$ and for U_e we take the average of the magnitude of the velocities in all integration points. In addition, a in the Eq. (18) is chosen equal to the polymer viscosity, $a = \eta_p$. We take the initial value $\boldsymbol{s}_0 = \boldsymbol{0}$, corresponding to zero initial stress.

The rigid-body motion on the particle boundary is imposed through Lagrange multipliers $\boldsymbol{\lambda}$ (see [35]). As a consequence, the particle kinematic quantities are considered as additional unknowns and are recovered by solving the full system of equations.

The particle motion is taken into account by using an ALE formulation (Arbitrarian Lagrange-Eulerian) [36,], whereby at each time step the mesh nodes are moved according to a grid velocity $\hat{\boldsymbol{u}}$ obtained by solving an extra equation. Notice that in general such node velocities are different from the fluid velocities at the nodes. This can be done until the mesh becomes too distorted. After that a new mesh is generated and the solution on the old mesh is projected onto the new one.

The node mesh movement is taken into account in the discretized form of the governing equations by subtracting the mesh velocity to the fluid velocity in the convective terms. In this regards, note that, due to the fluid inertialess assumption, the only convective term appears in the viscoelastic constitutive equation so in such a term (and in the test function), the velocity is actually $\boldsymbol{u} - \hat{\boldsymbol{u}}$. For the latter velocity we need an extra equation. Following [36], in order to guarantee a smooth mesh

motion, we use the Laplace equation:

$$\nabla \cdot (\epsilon \nabla \hat{\boldsymbol{u}}) = 0 \tag{24}$$

with boundary conditions:

$$\hat{\boldsymbol{u}} = \boldsymbol{U} + \boldsymbol{\omega} \times (\boldsymbol{x} - \boldsymbol{x}_p) \quad \text{on } \partial P(t) \tag{25}$$

$$\hat{\boldsymbol{u}} = \boldsymbol{0} \quad \text{on } \Gamma_i, \quad (i = 1...4) \tag{26}$$

In Eq. (24), the parameter ϵ is taken equal to the inverse of the local element area in order to let the largest elements adsorb the most part of deformation. Equations (25)-(26) assure that the particle boundary nodes move following the particle motion, whereas no movement is prescribed for domain boundary nodes. A weak form for Eq. (24) can be derived in a standard way.

The DEVSS-G/SUPG formulation with a log-representation of the conformation tensor and an ALE particle mover provides a very efficient method in order to handle the system under investigation, giving satisfactory results for all the set of parameters considered in this work.

4.2 Implementation

For the discretization of the weak form, we use triangular elements with continuous quadratic interpolation (P_2) for the velocity $\boldsymbol{u}$, linear continuous interpolation (P_1) for the pressure p, linear continuous interpolation (P_1) for velocity gradient $\boldsymbol{G}$ and linear continuous interpolation (P_1) for the log-conformation tensor $\boldsymbol{s}$.

Regarding the time discretization, we decouple the momentum balance and continuity equations from the constitutive one. As shown in the weak form, the mesh velocity, $\hat{\boldsymbol{u}}$, appears in the constitutive equation only. This allows us to solve separately the Laplace equation and the momentum balance.

Initially, the viscoelastic polymer stress is set to zero in the whole domain. Since we neglect inertia, the initial condition for the velocity is not necessary. So, we can solve the equations (18)-(20) and the constraint equation (22) in order to get the distribution of the fluid velocity and the rigid-body motion of the particles, at the initial time step. Then, at

every time step, we follow the following procedure:

Step 1. The particle position and rotation are updated. The new configuration is obtained by integrating the kinematic equation (15). The explicit second-order Adams-Bashforth method is used:

$$\boldsymbol{x}_p^{n+1} = \boldsymbol{x}_p^n + \triangle t \left(\frac{3}{2} \boldsymbol{U}_p^n - \frac{1}{2} \boldsymbol{U}_p^{n-1} \right) \tag{27}$$

The first time step of the simulation is performed with an explicit Euler method:

$$\boldsymbol{x}_p^{n+1} = \boldsymbol{x}_p^n + \triangle t \, \boldsymbol{U}_p^n \tag{28}$$

Step 2. The mesh nodes, $\boldsymbol{x}_m$, are updated according to:

$$\boldsymbol{x}_m^{n+1} = \boldsymbol{x}_m^n + \triangle t \, \hat{\boldsymbol{u}}^n \tag{29}$$

for the first time step and:

$$\boldsymbol{x}_m^{n+1} = \boldsymbol{x}_m^n + \triangle t \left(\frac{3}{2} \hat{\boldsymbol{u}}^n - \frac{1}{2} \hat{\boldsymbol{u}}^{n-1} \right) \tag{30}$$

when Eq. (27) is used to update particle position.

Step 3. The log-conformation tensor at the next time step, $\boldsymbol{s}^{n+1}$, is evaluated by integrating the constitutive equation (21). A second-order Crank-Nicolson/Adams-Bashforth scheme is used:

$$\begin{aligned} \frac{\boldsymbol{s}^{n+1}}{\triangle t} + \frac{1}{2}[(2(\boldsymbol{u}^n - \hat{\boldsymbol{u}}^n) - (\boldsymbol{u}^{n-1} - \hat{\boldsymbol{u}}^{n-1})] \cdot \nabla \boldsymbol{s}^{n+1} = \\ \frac{\boldsymbol{s}^n}{\triangle t} - \frac{1}{2}(\boldsymbol{u}^n - \hat{\boldsymbol{u}}^n) \cdot \nabla \boldsymbol{s}^n + \frac{3}{2} \boldsymbol{g}(\boldsymbol{G}^n, \boldsymbol{s}^n) - \frac{1}{2} \boldsymbol{g}(\boldsymbol{G}^{n-1}, \boldsymbol{s}^{n-1}) \end{aligned} \tag{31}$$

where $\boldsymbol{g}$ is the term which appears in the evolution equation of $\boldsymbol{s}$ (Eq. (17)). Notice that the velocity $\boldsymbol{u} - \hat{\boldsymbol{u}}$ in the convective terms is according to the ALE scheme. In the time integration scheme above, $2\boldsymbol{u}^n - \boldsymbol{u}^{n-1}$ and $2\hat{\boldsymbol{u}}^n - \hat{\boldsymbol{u}}^{n-1}$ are used as velocity predictions for $\boldsymbol{u}^{n+1}$ and $\hat{\boldsymbol{u}}^{n+1}$, respectively.

Step 4. The remaining unknowns $(\boldsymbol{u}, p, \boldsymbol{G}, \boldsymbol{U}_p, \boldsymbol{\omega})^{n+1}$ as well as the Lagrange multipliers $(\boldsymbol{\lambda})$ can be found by solving the Eqs. (18)-(20) and (22) using the particle configuration and the polymer stress evaluated in the previous two steps:

$$\int_W 2\eta_s \boldsymbol{D}(\boldsymbol{v}) : \boldsymbol{D}(\boldsymbol{u}^{n+1})\, dA - \int_W \nabla\cdot\boldsymbol{v}\, p^{n+1}\, dA + \int_W a(\nabla\boldsymbol{v})^T : \nabla\boldsymbol{u}^{n+1}\, dA$$
$$- \int_W a(\nabla\boldsymbol{v})^T : (\boldsymbol{G}^{n+1})^T\, dA + \langle \boldsymbol{v} - (\boldsymbol{V} + \boldsymbol{\chi}\times(\boldsymbol{x} - \boldsymbol{x}_p^{n+1}), \boldsymbol{\lambda}^{n+1}\rangle_{\partial P}$$
$$= -\int_W \boldsymbol{D}(\boldsymbol{v}) : \boldsymbol{\tau}_p^{n+1}\, dA, \quad (32)$$

$$\int_W q\nabla\cdot\boldsymbol{u}^{n+1}\, dA = 0, \quad (33)$$

$$\int_W \boldsymbol{H} : \boldsymbol{G}^{n+1}\, dA - \int_W \boldsymbol{H} : (\nabla\boldsymbol{u}^{n+1})^T\, dA = 0, \quad (34)$$

$$\langle \boldsymbol{\mu}, \boldsymbol{u}^{n+1} - (\boldsymbol{U}_p^{n+1} + \boldsymbol{\omega}^{n+1}\times(\boldsymbol{x} - \boldsymbol{x}_p^{n+1}))\rangle_{\partial P} = 0 \quad (35)$$

Step 5. Finally, the Laplace equation is solved:

$$\nabla\cdot(\epsilon\nabla\hat{\boldsymbol{u}}^{n+1}) = 0 \quad (36)$$

with boundary conditions:

$$\hat{\boldsymbol{u}} = \boldsymbol{U}^{n+1} + \boldsymbol{\omega}^{n+1}\times(\boldsymbol{x} - \boldsymbol{x}_p^{n+1}) \quad \text{on } \partial P(t) \quad (37)$$

$$\hat{\boldsymbol{u}} = \boldsymbol{0} \quad \text{on } \Gamma_i, \quad (i = 1...4) \quad (38)$$

and the mesh velocities are obtained.

In Step 4, a sparse linear symmetric system needs to be solved whereas Eq. (31) leads to an unsymmetric system. In both cases we use the parallel direct solver PARDISO [37,].

4.3 Node mesh updating

In principle the ALE method allows to use the starting mesh until it becomes too distorted. When this occurs, a new mesh covering the same domain of the old one is generated and the solution is projected from the old on the new mesh. The projection step is general done by interpolation: the element containing a new node is searched through the old mesh and, by using the nodal element values of the last solution, the fields are interpolated to give new nodal values. Such a procedure is time-consuming and leads to interpolation errors. Therefore it should be reduced as much as possible during the simulation.

Due to the particular geometrical system investigated in this work (a single circular particle in a channel), we may exploit the fact that the mesh velocities, $\hat{\boldsymbol{u}}$, can be chosen in an arbitrary way, and the projection step can be reduced to one-two times per simulation or even be avoided.

Indeed, as will be shown in Chapter 6.3.2, the particle moves along the $x-$direction, while translating along the $y-$axis very slowly (particle cross-streamline migration). This is equivalent to fix the particle along the $x-$axis and move the mesh nodes with an $x-$velocity given by the particle $x-$velocity, U_p. However, due to the periodicity along the $x-$axis, the new configuration (particle and mesh translated along the $x-$direction by a quantity related to the particle $x-$velocity) is equivalent to the one of the previous time step. It should be only recognized that the $x-$component of the mesh velocity is $\hat{u}_x = U_p$. Of course the particle can still move along the $y-$axis.

Therefore, such a procedure is implemented by solving in the Step 5 only the $y-$component of Eq. (24) and setting $\hat{\boldsymbol{u}} = (U_p, \hat{u}_y)$ in Eq. (31). In the Step 2 the mesh nodes are moved along the $y-$direction only and the mesh distortion is limited along the $y-$axis. Our simulations show that at most one-two remeshing and projection steps are needed.

Finally, regarding the mesh quality, following [36], we use two monitoring parameters:

$$f_1 = \max_{1 \leqslant e \leqslant N_{el}} (f_1^e) \quad \text{and} \quad f_2 = \max_{1 \leqslant e \leqslant N_{el}} (f_2^e) \tag{39}$$

where N_{el} is the number of elements and:

$$f_1^e = |\log(V^e/V_0^e)| \quad \text{and} \quad f_2^e = |\log(S^e/S_0^e)| \tag{40}$$

with V^e and V_0^e the volume of the element e and its value in the undeformed configuration, respectively; S^e and S_0^e are the aspect ratios of the element e and its value in the undeformed mesh, respectively. The aspect ratio is defined as:

$$S^e = \frac{(l^e)^3}{V^e} \tag{41}$$

with l^e the maximum length of the sides of the element e.

As soon as one of f_1 or f_2 is greater than 1.39 (i.e. element volume or aspect ratio is larger than four times or smaller than 1/4 of its original value) the mesh is considered too distorted and needs to be regenerated.

5 Convergence and code validation

5.1 Code validation

The method proposed (DEVSS/SUPG + ALE) is validated through a comparison with the fictitious domain method (FDM) [38,]. In the latter, a regular mesh is used covering the fluid as well as the solid domain. The particle rigid-body motion is imposed inside the particle (or on its boundary if inertia is neglected [39, 40]) through Lagrange multipliers. The details of the fictitious domain method used in this work (weak form and implementation) are reported in [35] with the only difference that here we used a weak implementation of rigid-body constraints instead of collocation [41]. We just give a brief description of the mesh used: since the particle moves along the $x-$direction because of the external flow field and migrates slowly approaching the closest wall, the regular mesh used is refined in a narrow channel where the particle is expected to move. As soon as the particle, due to the migration along the $y-$direction, is going out the refined channel, a new mesh is generated by translating the channel (that, of course, partially covers the refined region of the previous mesh). The solution is then projected from the old to the new mesh. In such a way, we can concentrate elements where the particle is moving. Considering that the projection is done at most 3-4 times in a simulation, the accuracy is not compromised at all.

In figure 5 (left) the comparison between the two methods is done by considering the particle $y-$position as function of time. A good quantitative agreement is found for any particle starting position.

The FDM predictions are always slightly higher then the ALE ones. As indeed is evident in figure 5 where V_p vs time are reported (right), whereas a monotonic curve (initially decreasing and then increasing) is found for V_p in the ALE method, oscillations are evident when the FDM is considered. Such oscillations are due to the relative motion of the particle boundary grid over the fixed grid. In general, the error is small but in the problem investigated V_p is small as well and this results in strong oscillations around the exact value. Finally, considering that the oscillations are on average above the curve for ALE, the trajectories reported on the left of figure 5 can be justified. To decrease the velocity perturbations a further mesh refinement is needed and the dashed curves

are expected to tend to the solid one.

To close the comparison between ALE and FDM, it must be taken into account the computational aspect as well. Our FDM simulations requires a calculation time about 10 times higher than the ALE method. This is quite easy to understand if one considers that the refinement around the particle is more effective when a boundary fitted mesh is implemented and an irregular, coarse mesh can be done far from the particle. On the other hand, the FDM mesh should satisfy some regularity far from the particle as well, limiting its coarseness. In conclusion, the problem of a single particle in a rectangular box is more effectively tackled by using a boundary fitted method. Instead, for a many particle system, where frequent remeshing and projection steps are required, along with the difficulties related to the mesh generation itself, it is preferable using a fictitious domain method, maybe together with a proper algorithm deforming and refining the regular mesh along the particle boundaries.

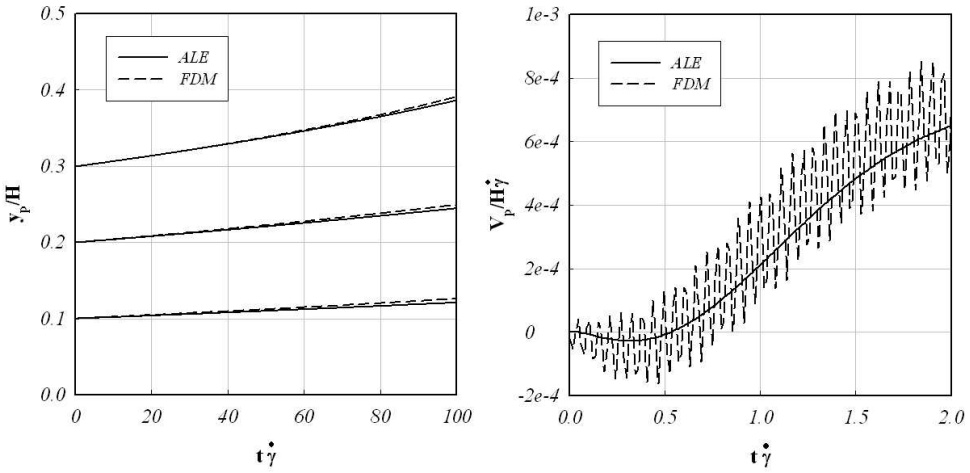

Figure 5: $y-$position of particle center (y_p) (left) and particle $y-$velocity (V_p) (right) for ALE method (solid lines) and fictitious domain method (dashed line).

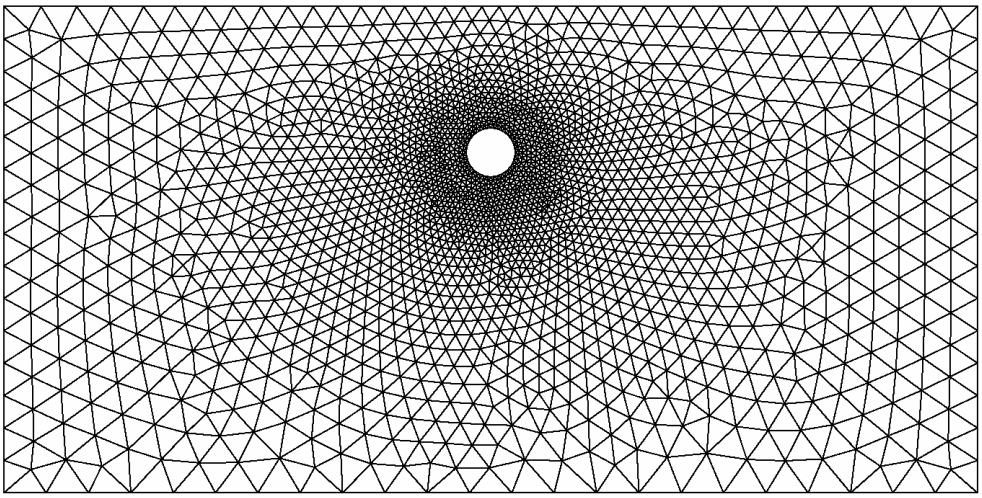

Figure 6: Typical mesh used in the simulations. The mesh reported is the one labeled as 'M1' in Table I.

5.2 Convergence in space and time

In this Section, the results about the convergence in space and time of our method are presented. In what follows, we report a limited set of example cases in order to show the sensitivity of the method implemented to mesh resolution and time step size. However it must be remarked that the convergence is checked for any fluid and geometrical parameter presented in this work.

In the following chapter we will present our results on the migration of a single particle under continuous shear flow, under oscillatory shear flow and on the effect of curvature on migration. For the three situation investigate we use different geometries.

5.2.1 Convergence in space and time in the case of continuous shear flow

In figure 6 it is shown a typical mesh used in the simulations. The channel length (L) is chosen sufficiently large to avoid that the particle can feel itself through the periodic boundaries. Notice the refinement around the particle and between the particle and the closest wall, where largest gradients are expected.

Mesh label	#el. on the particle boundary	#el. in the mesh
$M1$	40	4176
$M2$	50	6096
$M3$	60	8012
$M4$	80	12978

Table 1: Mesh parameters (for $D_p/H = 0.1$ and $y_{p,0} = 0.2$)

The spatial convergence is checked by refining the mesh. In Table 1, some parameters of the mesh used are reported. The mesh in figure 6 is the one labeled as 'M1' (the coarsest one). The meshes in the table refer to a specific particle size and starting position. However, the number of elements is kept almost the same by changing the geometrical parameters.

In figure 7 the angular velocity, ω, and the particle $y-$velocity, V_p, of a particle starting from $y_{p,0} = 0.3$ are reported for the meshes labeled as 'M1', 'M2', 'M3' and 'M4'. The step size chosen is 0.01 and the other parameters are: $De = 1.0$, $\alpha = 0.2$, $\eta_s/\eta_p = 0.1$, $D_p/H = 0.1$.

The start-up as well as the long-time behavior are correctly predicted by all the meshes investigated. The convergence is achieved for the mesh 'M3', although the comparison with 'M1' and 'M2' leads to very small deviations ($\cong 2 \div 3\%$ for V_p and $\cong 0.5 \div 1\%$ for ω). A similar situation is found for $De = 2.0$ (not reported). However, we remark that the convergence is strictly depending on the fluid and geometrical parameters. In general, our convergence tests show that a finer mesh is needed as Deborah number increases (for $De = 3.0 \div 4.0$ we need the mesh 'M4') and as α is reduced (the Giesekus model tends to the Maxwell one that gives well-known convergence problems). On the other hand, for different particle sizes, leading of course to a different spatial distribution of triangles, about the same number of elements are sufficient to achieve the convergence.

Finally, the influence of time step size, Δt, is investigated. We consider the mesh 'M3' and $De = 1.0$. In figure 8, V_p and ω by varying Δt are considered. Even for the largest Δt considered, the curves superimpose. However, for $\Delta t = 0.02$ (dotted line), slight deviations are found in the start-up phase (see the inset on the right of figure 8) that are more and more pronounced as the particle starts close to the wall (such an

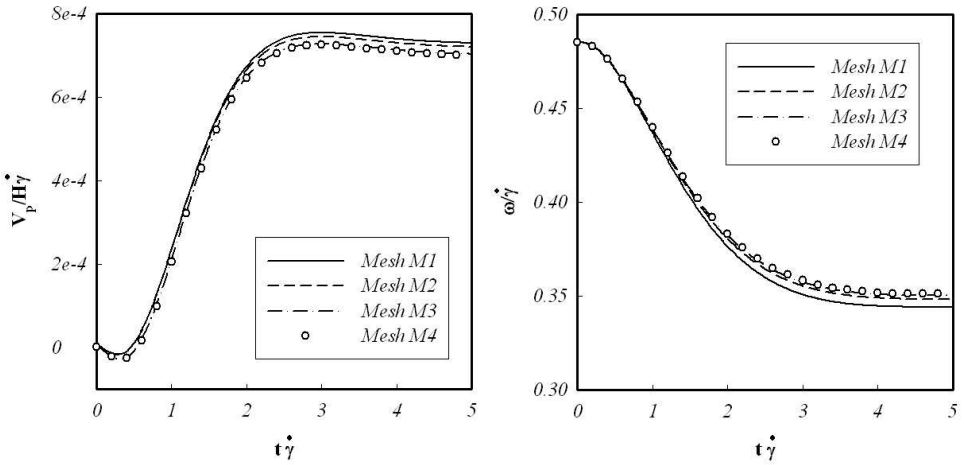

Figure 7: Particle $y-$velocity (V_p) (left) and angular velocity (ω) (right) as functions of time for the meshes reported in Table I.

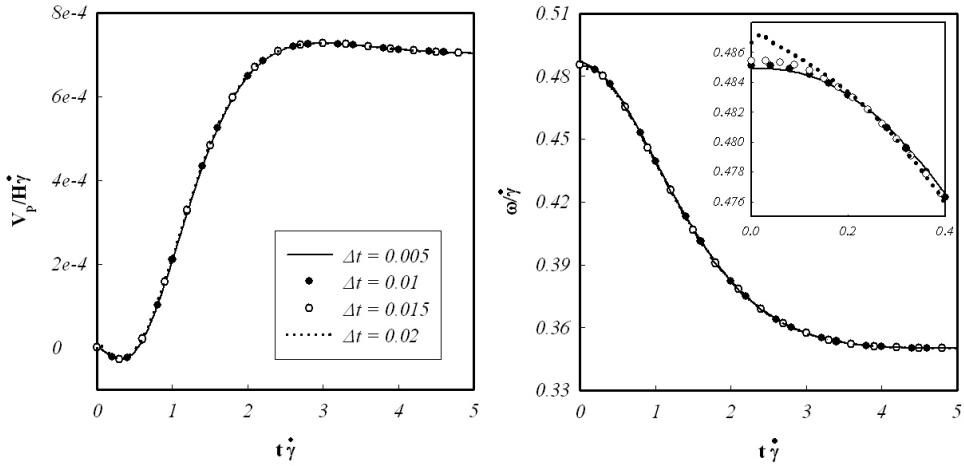

Figure 8: Particle $y-$velocity (V_p) (left) and angular velocity (ω) (right) as functions of time for different time step size (Δt).

Mesh label	#el. on the particle boundary	#el. in the mesh
$M1$	80	12463
$M2$	100	15729
$M3$	120	18530

Table 2: Mesh parameters (for $D_p/H = 0.18$ and $y_{p,0} = 0.3$)

effect has been reported in [42] and [43] too). On the other hand, by changing fluid and geometrical parameters, we do not find any different behavior with respect to the one shown in figure 8. For these reasons, in all simulations in this work, Δt is chosen 0.015, being a good compromise between simulation speed and accuracy.

5.2.2 Convergence in space and time in the case of oscillatory shear flow

The second aspect we want to investigate is the effect of oscillation on particle migration. As written in chapter 6.2 we want to compare our result with the experimental data of Lormand and Phillips, so our geometrical parameters are chosen in order to respect the ratio D_p/H used in the experiment. Thus, these simulations are performed in a 2D rectangular domain (which dimensions are H=1 and L=3) and D_p=0.18. Also in this case, the length of the domain is chosen so that the particle do not interact with itself during the motion thorough the periodical boundaries. In this case the plates move with a square wave which is characterize by two parameters: the amplitude A and the frequency f.

In table 2 the parameters of the tested meshes are reported

In figure 9 the $y-$ position of the particle and the $y-$velocity of the particle vs time are reported. The suspending fluid is a Giesekus fluid with these values for the parameter $\lambda = 0.2$, $\alpha = 0.2$, $\eta_s/\eta_p = 0.1$, $\Delta t = 0.005$. The parameters of the square wave are $A = 5$ and $f = 0.1$. As the particle is described by an higher number of elements, we do not find relevant differences between the results obtained with the different meshes. So for these set of simulations we chose the mesh M1 described in Table II. Notice that also in these case the convergence depends on the suspending fluid parameters and, furthermore, on the square wave

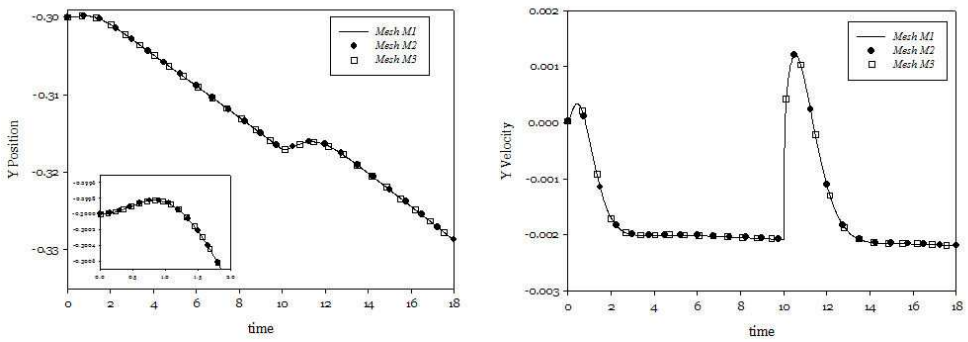

Figure 9: Particle $y-$position (left) and $y-$velocity (right) as functions of time for the meshes reported in Table 2.

parameters. In particular, we will choose a finer mesh if we need to decrease the values of A and f.

Also in this case we check the mesh convergence in time (see Fig 10). We find that the convergence is achieved also for large values of Δt. For these simulations, performed by using the mesh "M1" described before, the other parameters are $\lambda = 0.2$, $\alpha = 0.2$, $\eta_s/\eta_p = 0.1$. These results allow us to fix $\Delta t = 0.015$ for all the simulations described in Chapter 6.2

5.2.3 Convergence in space and time in the case of couette flow

The third aspect on we will discuss in Chapter 6.3 is the effect of curvature on the migration of the particle. In order to do that we perform a set of simulation on the 2D domain described in figure 11.

The side Γ_1 is the moving one, the side Γ_3 is steady. On the sides Γ_2 and Γ_4 we impose equal radial velocities and opposite tangential velocities.

Before testing the convergence of the mesh, we want to ensure that we can use such geometry in our simulations. So we run a set of simulation of a Newtonian fluid between two concentric cylinders in absence of particle. Then we compare the velocity profile as a function of the radius obtained by the simulations and from the analytical solution.

In figure 12 the comparison between our data (triangles) and the

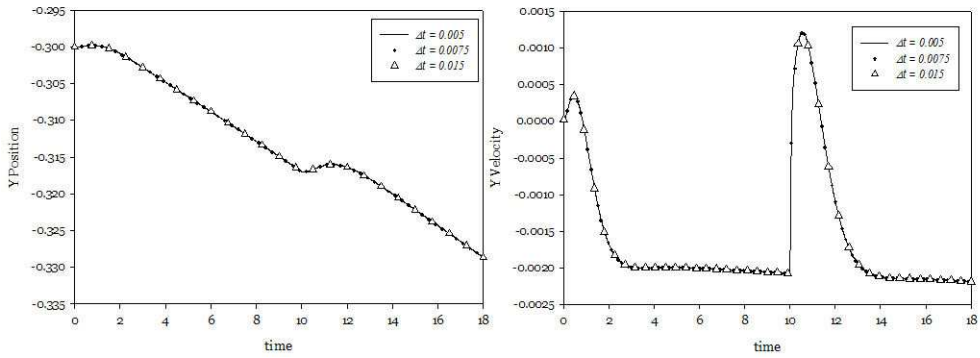

Figure 10: Particle $y-$position (left) and $y-$velocity (right) as functions of time for different values of Δt.

analytical solution (solid line) is reported: there is a perfect overlap between the two curves. We want to emphasize that this result is valid for any radius, in fact we compared also the values of velocity in every point of the mesh with the values obtained in the same point by the analytical solution. The maximum deviation between the two predictions is 10^{-6}.

As done before, we check the convergence in space and time for this new geometry. In all the case investigated, our mesh is finer near the particle for a better accuracy. In table 3 we report some parameters of the meshes we use for testing

The geometrical parameters are: $R_i = 20$, $R_e = 21$, $D_p = 0.12$. Also in this case these parameters are chosen in order to respect the ratio D_p/R_i and D_P/H (H is the gap between the two cylinders i.e. $R_e - Ri$)

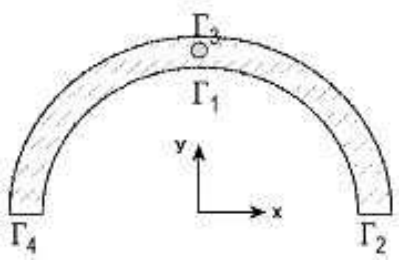

Figure 11: Schematic representation of the domain. The origin of a Cartesian frame is located at the center of the two cylinders.

Mesh label	#el. on the particle boundary	#el. in the mesh
$M1$	80	9386
$M2$	100	13312
$M3$	120	17950
$M4$	140	20436

Table 3: Mesh parameters (for $D_p/H = 0.12$ and $y_{p,0} = 20.5$)

used in the experiments of Lormand and Phillips. The suspending fluid is a Giesekus fluid which parameters are $\lambda = 0.2$, $\alpha = 0.2$, $\eta_s/\eta_p = 0.1$. In this case we define the shear rate $\dot{\gamma}$ as follows

$$\dot{\gamma} = \frac{\Omega R_i}{R_e - Ri} \tag{42}$$

Notice that in case of couette flows, the shear rate is not constant in the gap due to the curvature. The shear rate defined in Eq. (42) refers to the inner cylinder. We imposed $\dot{\gamma} = 3$.

Also in this case we can define Deborah number as $De = \lambda\dot{\gamma}$ with $\dot{\gamma}$ defined as in Eq. (42).

In figure 13 the radial position of the particle and its migration ve-

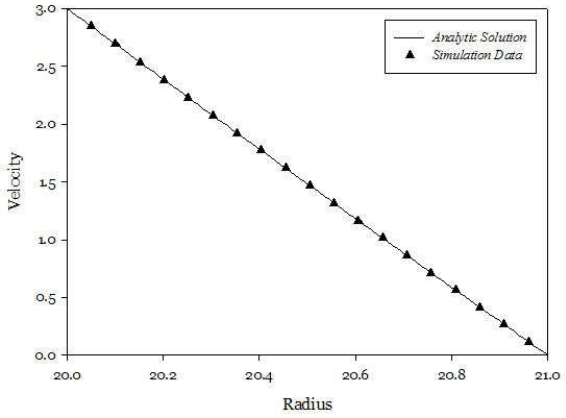

Figure 12: Velocity profile between two concentric cylinders. Comparison between the analytic solution and the simulation data

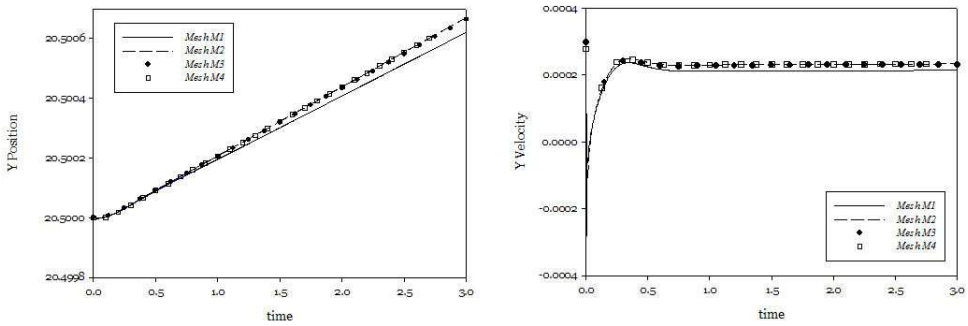

Figure 13: Particle radial position (left) and radial velocity (right) as functions of time for the meshes reported in Table 3.

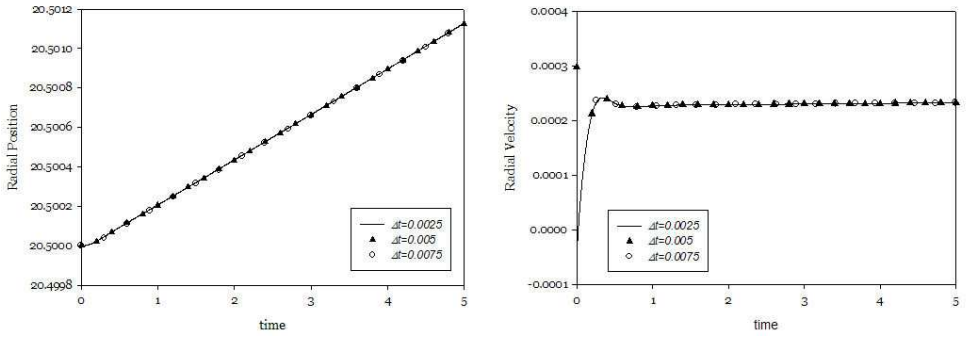

Figure 14: Particle radial position (left) and radial velocity (right) as functions of time for different values of Δt.

locity are plotted vs time for the differen meshes. Mesh convergence is achieved for mesh "M3". Also in these case we can notice very small deviations from the data obtained with the mesh "M1". Notice that the convergence of the mesh is influenced not only by the suspending fluid used in simulations, but also by the curvature: in fact we need a finer mesh if we increase the curvature of the cylinders.

Finally, we investigate the time convergence for mesh "M3" (see Fig. 14). The other parameters are $\lambda = 0.2$, $\alpha = 0.2$, $\eta_s/\eta_p = 0.1$, $\dot{\gamma} = 3$. Notice that, also in this case the convergence in time is reached also for high values of Δt. For all the cases investigated under couette

flow, we fix $\Delta t = 0.005$.

6 Simulation results

In this Section our simulation results are presented and discussed. This chapter is divided as follows: in the first part we show our simulation results on the particle migration under continuous shear flow and we analyze the effect of the particle size and of the suspending fluid on migration. Then we study the migration under oscillatory shear flow and we compare our results with the experimental data of Lormand and Phillips[29]. Finally, in the third part, we analyze the effect of curvature on particle migration.

6.1 Migration of particle under continuous shear flow

As stated in Section 5, the time step size $\Delta t = 0.015$ provides time convergent solutions for any case investigated in this work. On the contrary, the mesh size is strongly dependent on the fluid and geometrical parameters. The spatial convergence is therefore checked for all the situations investigated. For these sets of simulations the length of the domain is $L = 2$

In figure 15, the $y-$position of the particle center y_p as function of time is reported for different starting positions $y_{p,0}$. The parameters chosen are: $De = 1.0$, $\alpha = 0.2$, $\eta_s/\eta_p = 0.1$ and $D_p/H = 0.1$. Due to the symmetry with respect to the centerline (at $y = 0$), the trajectories are symmetric as well, and only one-half domain ($y \geq 0$) is considered. The shaded region in the upper part delimits the channel zone where the particle cannot access because of its finite size: when the particle center is at $y = 0.45$, the particle touches the wall.

The trends in figure 15 show that, from any starting position, the particle moves towards the closest wall (the upper one). Of course, due to the symmetry mentioned above, a particle initially located with the center exactly at the channel centerline will stay there and only rotate. Notice also that, close to the upper wall ($y_p > 0.3$), the trajectories are steeper than those in the channel core, i.e., the particle migration is faster near to the walls. What is found here is completely different from the case of an inertialess Newtonian suspending fluid where no migration occurs, independently of the initial position. Finally, note that the curves do not

touch the shaded region because our numerical method breaks down as soon as the particle is about $1/5D_p$ from the wall. The analysis of the situation of a particle touching the wall is beyond the scope of this work and requires different techniques of analysis.

Particle $y-$velocities (migration velocities), V_p, are reported in figure 16 and the angular velocities, ω, are plotted in figure 17.

In both figures, after an initial transient due to the development of viscoelastic stresses, the kinematic quantities change slowly in time for particle near to the channel center, and at a slightly faster pace for particles nearer to the walls. In other words, in the system under investigation no steady state is ever achieved and the particle motion is always transient in nature. Exceptions are a particle located on the channel

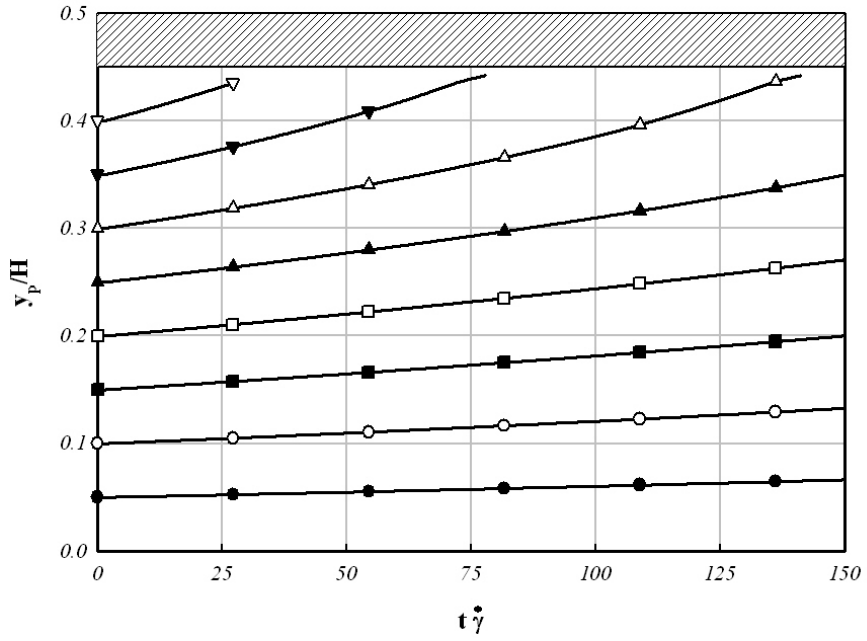

Figure 15: $y-$position of particle center (y_p) as a function of time (t) for different starting positions ($y_{p,0}$). The other parameters are: $De = 1.0$, $\alpha = 0.2$, $\eta_s/\eta_p = 0.1$, $D_p/H = 0.1$. The shaded area is the channel region unaccessible to the particle due to its finite size.

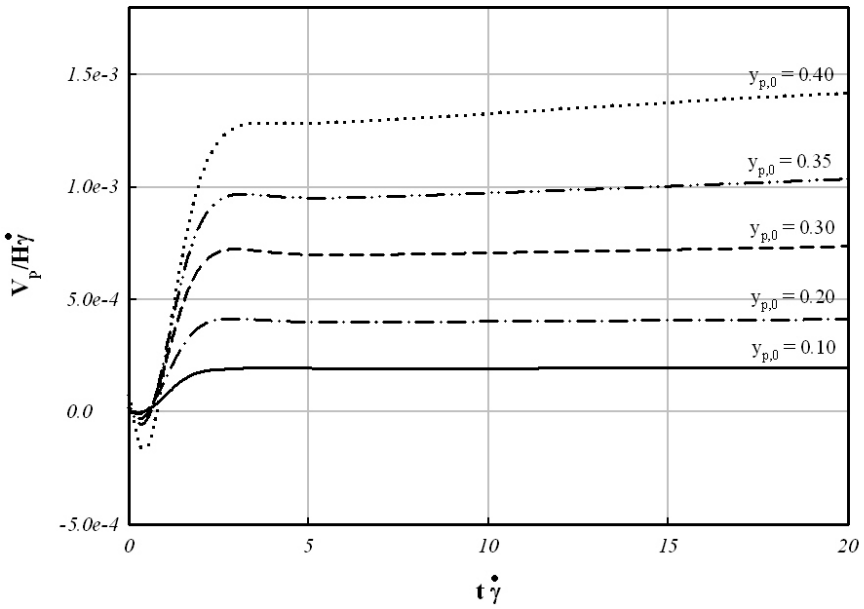

Figure 16: Particle migration velocities (V_p) as a function of time (t) for different starting positions ($y_{p,0}$). The other parameters are: $De = 1.0$, $\alpha = 0.2$, $\eta_s/\eta_p = 0.1$, $D_p/H = 0.1$.

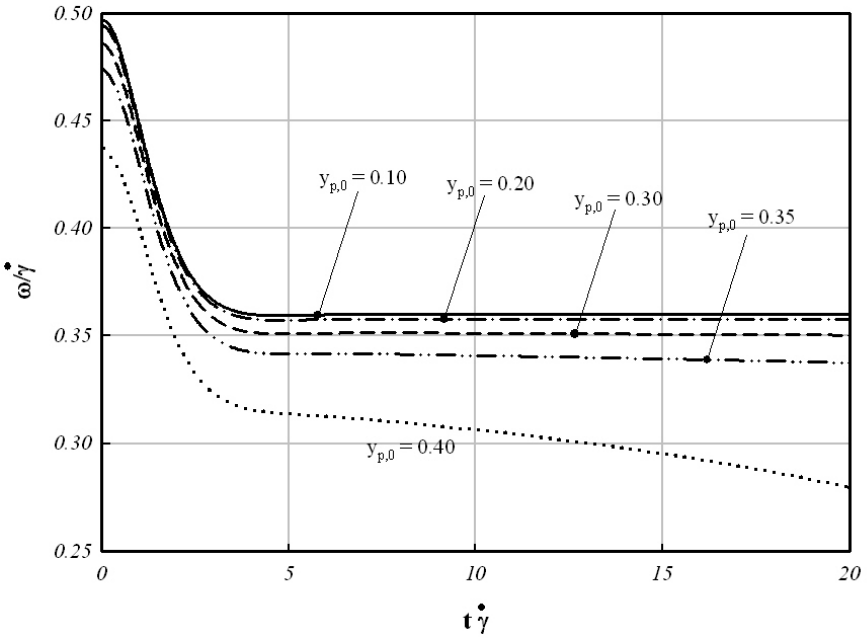

Figure 17: Particle angular velocities (ω) as a function of time (t) for different starting positions ($y_{p,0}$). The other parameters are: $De = 1.0$, $\alpha = 0.2$, $\eta_s/\eta_p = 0.1$, $D_p/H = 0.1$.

centerline and a particle that reaches the wall. The outwardly directed migration can then be looked at as an instability of the dynamics at the centerplane: when the particle center of mass is midway between the walls, no transverse motion occurs, but any disturbance in the vertical position triggers the migration. A very similar instability was very recently experimentally observed by [44] in pressure-driven flow of a bubble suspended in a viscoelastic liquid in microchannels.

The dynamics of the particle so far described is determined by the three state variables position, migration velocity, and angular velocity, reported as a function of time in figures 15, 16, 17 respectively. It is instructive to analyze such dynamics directly in the 'phase space' of the particle, i.e., the space formed by the state variables only. This is done in figures 18 and 19 where V_p and ω, respectively, are reported versus the vertical position.

For the sake of clarity, the fast initial dynamics has not been used in figures 18-19. The symbols in figures 18-19 refer to different starting positions, with the same symbology of figure 15. Notice that symmetry with respect to midplane dictates the parity (oddity) of the function $\omega(y)$ ($V_p(y)$), and for this reason only the upper half channel is shown in figures 18-19. Concerning the migration velocity shown in figure 18, we may note that: i) all the data collapse onto a single curve, regardless the starting position, ii) in the channel core the migration velocity scales linearly with position (see later), iii) by approaching the wall a faster migration is observed, iv) the curve passes through a maximum to abruptly decrease very near to the wall. In short, three different dynamics can be distinguished pertaining to three different zones of the channel.

Concerning the angular velocity ω in figure 19, again data collapse on a single curve (when disregarding the initial transients), and different dynamics are found in different channel regions. In particular, notice the steep decrease of the angular velocity when approaching the wall.

The data reported in figure 18-19 are well described by the following functional forms:

$$V_p = m_1\, y_p + m_5\, y_p^5 \tag{43}$$

$$\omega = a_0 + a_2 y_p^2 + a_n y^n \tag{44}$$

Some remarks: i) the constant term in Eq. (43) is missing because of the symmetry around the channel centerline ($y_p = 0 \Rightarrow V_p = 0$), ii) the linear

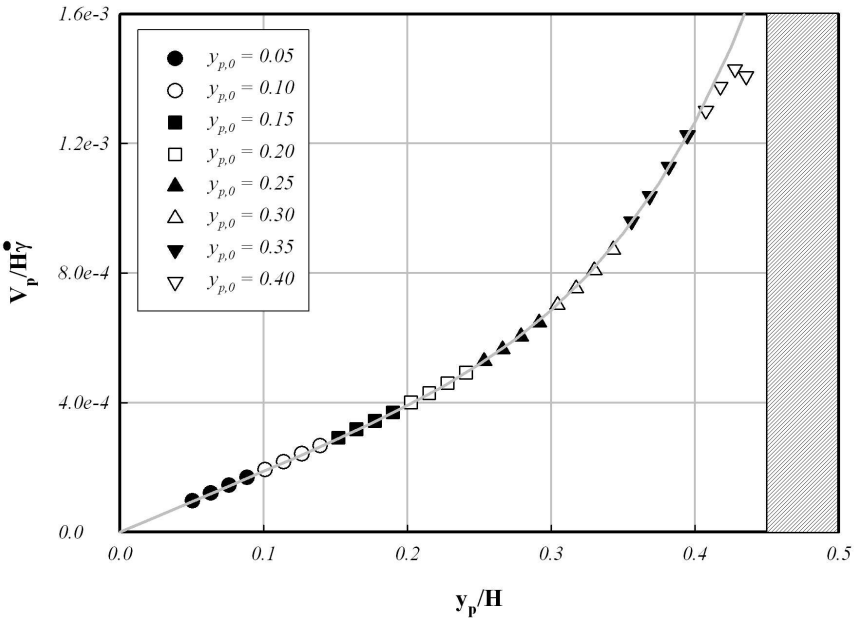

Figure 18: Particle migration velocities (V_p) as a function of particle $y-$positions (y_p) for different starting positions ($y_{p,0}$). The other parameters are: $De = 1.0$, $\alpha = 0.2$, $\eta_s/\eta_p = 0.1$, $D_p/H = 0.1$. The same symbology of figure 15 is used. The grey line is the function reported in Eq. (43). The shaded area is the channel region unaccessible to the particle due to its finite size.

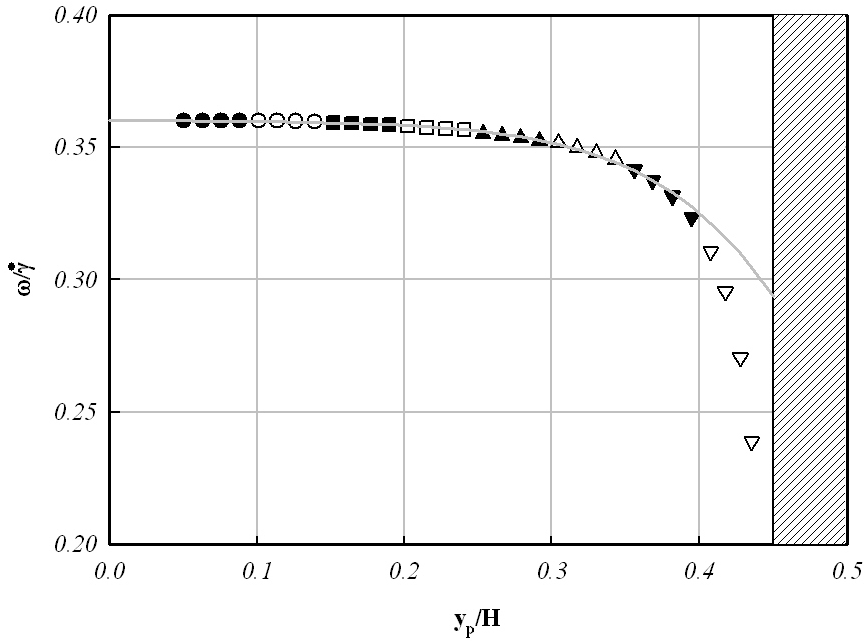

Figure 19: Particle angular velocities (ω) as a function of particle $y-$positions (y_p) at different starting positions ($y_{p,0}$). The other parameters are: $De = 1.0$, $\alpha = 0.2$, $\eta_s/\eta_p = 0.1$, $D_p/H = 0.1$. The same symbology of figure 15 is used. The shaded area is the channel region unaccessible to the particle due to its finite size.

term in Eq. (43) governs the dynamic in the core regime, iii) the constant term in Eq. (44) is the angular velocity of a particle at the center plane under confined shear flow (compare with [43]).

It should be pointed out that the functions (43) and (44) do not come from any theory or physical consideration but are just the best polynomial fits the simulation data. Indeed, we remark that the fitting polynomials will be different with different choices of D_p/H, De and α (see below), not only in terms of coefficients but even in power laws. Independently from those geometrical and fluid parameters, however, the functional forms in the core region ($y/H << 1$) are found to be universal, i.e., it is always $m_0 = 0$, $m_1 \neq 0$, $a_0 \neq 0$, $a_2 \neq 0$. Notice that for fitting the migration velocity we excluded the last 4 points because Eq. (43) cannot be used to predict the decreasing trend very close to the wall.

The functional form, Eq. (43), can be integrated to recover the particle trajectory in time over the channel:

$$\frac{dy_p}{dt} = V_p = m_1\, y_p + m_5\, y_p^5 \qquad \Longrightarrow \qquad y_p = \frac{y_{p,0}\, m_1^{1/4} \exp(m_1 t)}{[m_1 + y_{p,0}^4\, m_5 (1 - \exp(4 m_1 t))]^{1/4}} \tag{45}$$

with initial condition $t = 0 \Rightarrow y_p = y_{p,0}$. The meaning of m_1 coefficient is apparent from Eq. (45): indeed, it represents the growth rate of the instability from the center line [44,]. Eq. (45) is the master curve governing the particle trajectories in the whole channel (excluded the terminal part). In other words, the behavior in the core regime as well as wall regime is completely defined by Eq. (45) regardless the starting position. Notice that the core regime is governed by an exponential-like trajectory as follows by setting $m_5 = 0$ in Eq. (45).

In figure 20, Eq. (45) is reported with a grey line. The symbols refer to the curves calculated through numerical simulations reported in figure 15. The overlap for any starting position $y_{p,0}$ confirms the validity of Eq. (45) in the whole channel (except the terminal region): in conclusion, each individual trajectory, just translated in time, is a part of an unique behavior.

Finally, we emphasize once more that such a relationship is not valid in the initial transient behavior due to the development of fluid stresses. However, as evident in figure 16 or 17, 3-4 relaxation times are sufficient to extinguish the initial start-up and entering the slow dynamics.

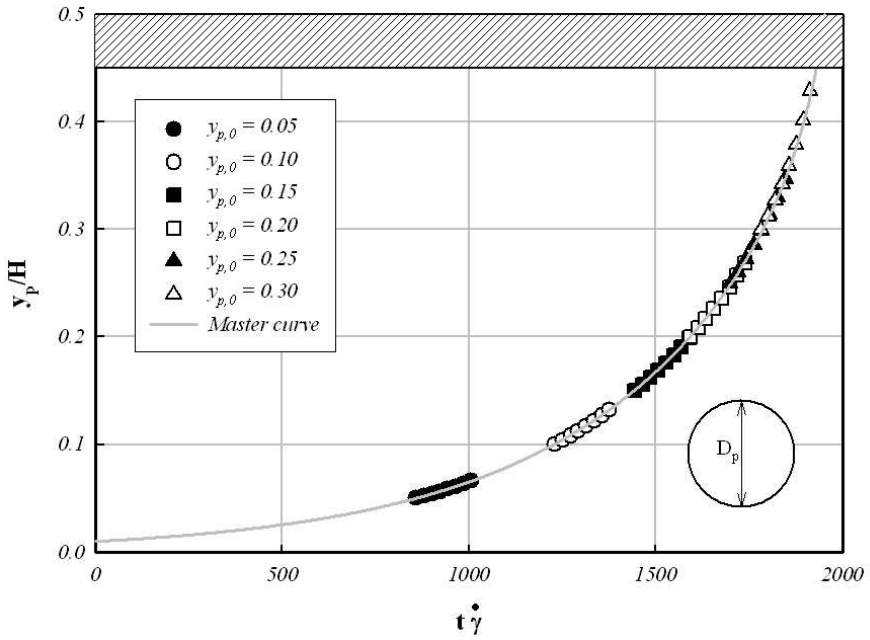

Figure 20: Master curve given by Eq. (45) (grey line) and the simulated trajectories reported in figure 15 (symbols). The parameters are: $De = 1.0$, $\alpha = 0.2$, $\eta_s/\eta_p = 0.1$, $D_p/H = 0.1$. A representation of the particle is reported as well. The shaded area is the channel region unaccessible to the particle due to its finite size. In the figure is also reported a schematic representation of the particle, for $D_p/H = 0.1$, to show its dimension compared to the channel size.

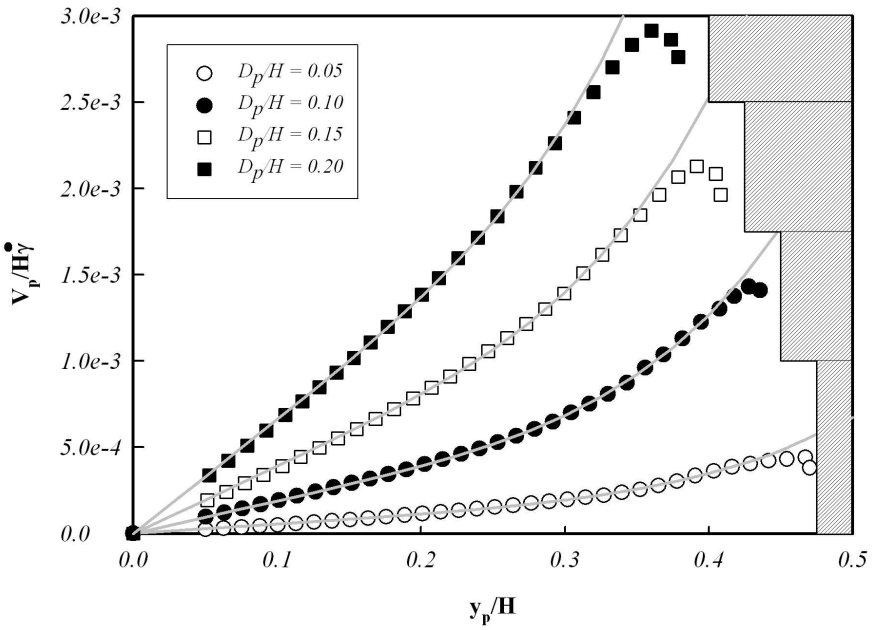

Figure 21: Particle migration velocities (V_p) as a function of particle $y-$positions (y_p) for different D_p/H values. The other parameters are: $De = 1.0$, $\alpha = 0.2$, $\eta_s/\eta_p = 0.1$. The grey lines are the functions reported in Eq. (43) with the parameters calculated by fitting the simulation data. The shaded area is the channel region unaccessible to the particle due to its finite size (depending on the particle size).

The just discussed master curves depend on D_p/H ratio and fluid parameters (De and α). In the following, the effects of geometrical and fluid parameters are separately investigated.

6.1.1 Effect of particle size

The influence of the particle size is investigated by varying D_p/H ratio (dimensionless diameter) at $De = 1$ and $\alpha = 0.2$. In figure 21 the particle $y-$velocity V_p is reported as a function of particle $y-$position y_p for 4 different D_p/H values.

The full circles refer to $D_p/H = 0.10$ and are the same data as in fig-

ure 18. The three different regimes identified in the previous section, the core, the intermediate and the close-wall regimes, exist even by varying the confinement. We notice that a stronger confinement (higher D_p/H) leads to a faster migration in the whole channel, in particular, the instability growth rate monotonically increases by increasing the dimensionless diameter, following a quadratic law. For whatever dimensionless diameter, however, simulation data are still very well fitted by the functional form in Eq. (43). The fitting curves (with the two parameters m_1 and m_5 evaluated by a least square method) are reported as grey lines in the figure. It is apparent that the curves well describe the particle dynamic except very near to the wall.

The validity of Eq. (43) for any D_p/H ratio investigated implies that the particle trajectories are in the form of Eq. (45). Such curves are reported in figure 22 (for $y_{p,0} = 0.05$) where the faster migration at stronger confinement is evident.

Coming back to the three dynamical regimes mentioned above, figure 23 summarizes their sizes, (H^*), as the dimensionless diameter is varied. The separatrix between the core and intermediate regimes is identified by those data in figure 21 showing a deviation of 5% from the linear trend. The separatrix between the intermediate and the close-wall regimes is identified by 5% deviations of data from the grey curves in the same figure. Notice that the core regime covers the most part of the channel especially as the confinement is weak, whereas the close-wall regime becomes larger and larger as the confinement is stronger.

6.1.2 Effect of fluid rheology

The effect of Deborah number is now investigated, at a fixed $D_p/H = 0.1$. In figure 24 the migration velocities as a function of the particle $y-$position are reported for different De values. The black circles are the same data as in figure 18. It is immediately evident that the overall migration behavior is still found, i.e. we distinguish the linear core regime, a faster intermediate regime and a close-wall regime. Furthermore, the transitions among those three dynamics seems to be independent of Deborah number (for example look at the maxima of the curves).

An important effect of the $De-$value is the non-monotonic behavior of the instability growth rate visible in figure 24. Indeed, the slope of the

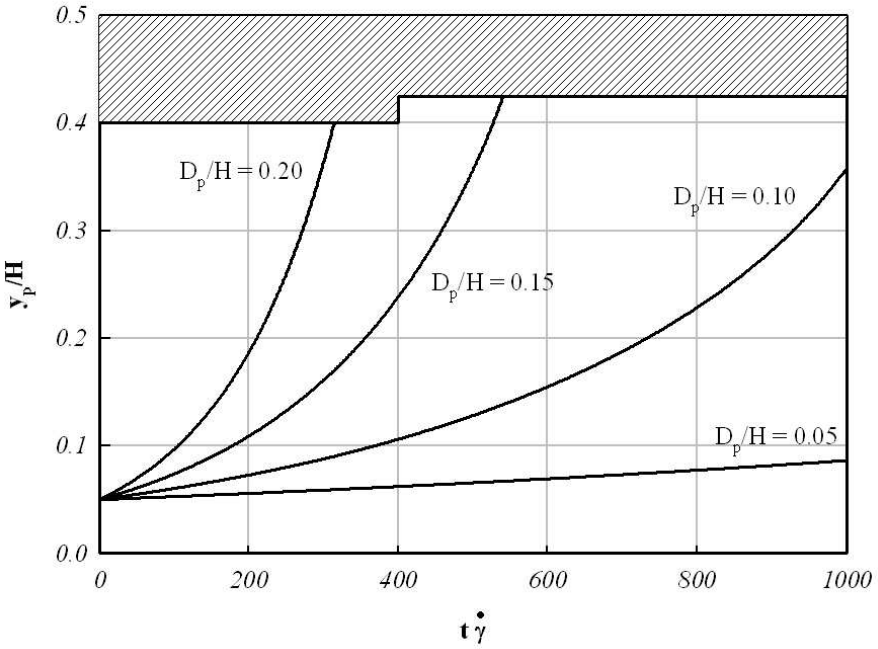

Figure 22: $y-$position of particle center (y_p) as a function of time (t) for different D_p/H ratio. The other parameters are: $De = 1.0$, $\alpha = 0.2$, $\eta_s/\eta_p = 0.1$. The shaded area is the channel region unaccessible to the particle due to its finite size (depending on the particle size).

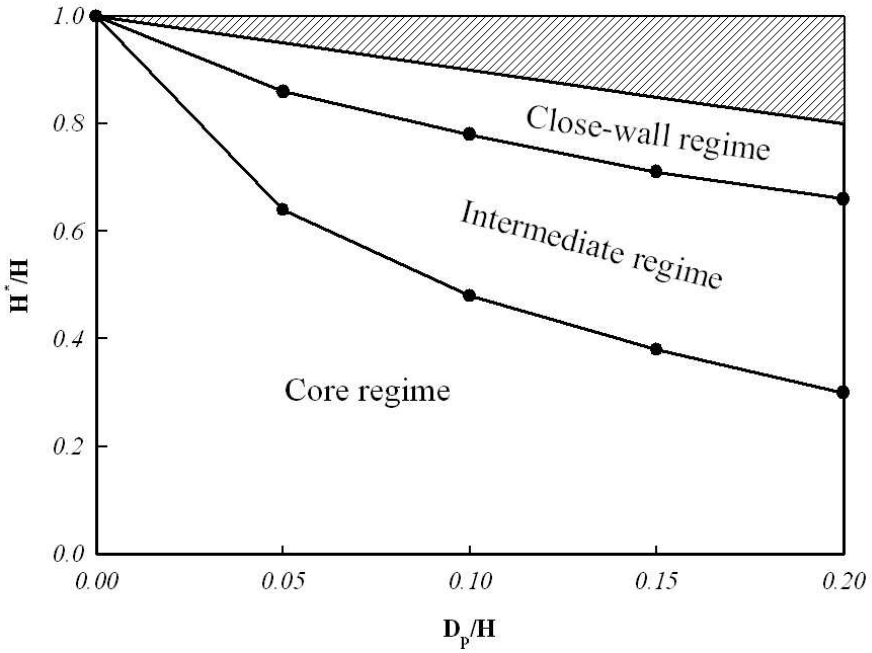

Figure 23: Dimensionless channel size (H^*/H) versus D_p/H. The curves delimit the core, the intermediate and the close-wall regime. The shaded area is the channel region unaccessible to the particle due to its finite size (depending on the particle size). The other parameters are: $De = 1.0$, $\alpha = 0.2$, $\eta_s/\eta_p = 0.1$.

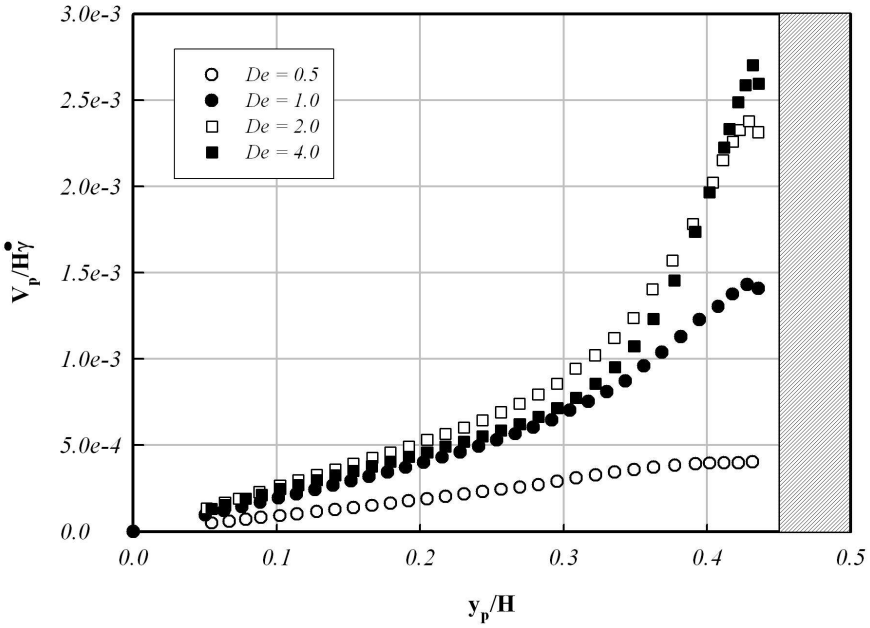

Figure 24: Particle migration velocities (V_p) as a function of starting positions ($y_{p,0}$) for different Deborah numbers (De). The other parameters are: $\alpha = 0.2$, $\eta_s/\eta_p = 0.1$, $D_p/H = 0.1$.

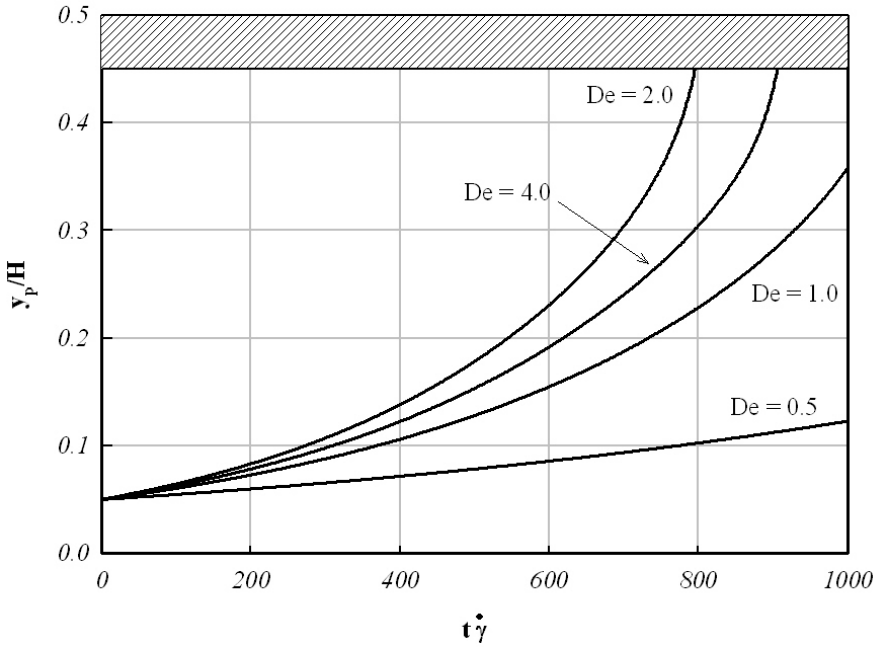

Figure 25: $y-$position of particle center (y_p) as a function of time (t) for different Deborah numbers (De). The other parameters are: $\alpha = 0.2$, $\eta_s/\eta_p = 0.1$, $D_p/H = 0.1$.

migration velocity curve in the core regime first increases with De. The curve for $De = 4.0$ (black squares), however, lies in between those for $De = 1.0$ (black circles) and $De = 2.0$ (white squares). As a consequence, beyond some critical $De-$number (larger than unity), a particle moving in the central channel region migrates increasingly slower as De increases.

In the intermediate regime, on the other hand, the migration velocity increases monotonically with De. This latter behavior implies that the functional form in Eq. (43) cannot be used to describe the data in figure 24. Indeed, although the linear term is always present, the exponents of the nonlinear terms vary with De.

The just described dependence on De of the migration velocity is perhaps more evident by looking directly at particle trajectories, as shown in figure 25.

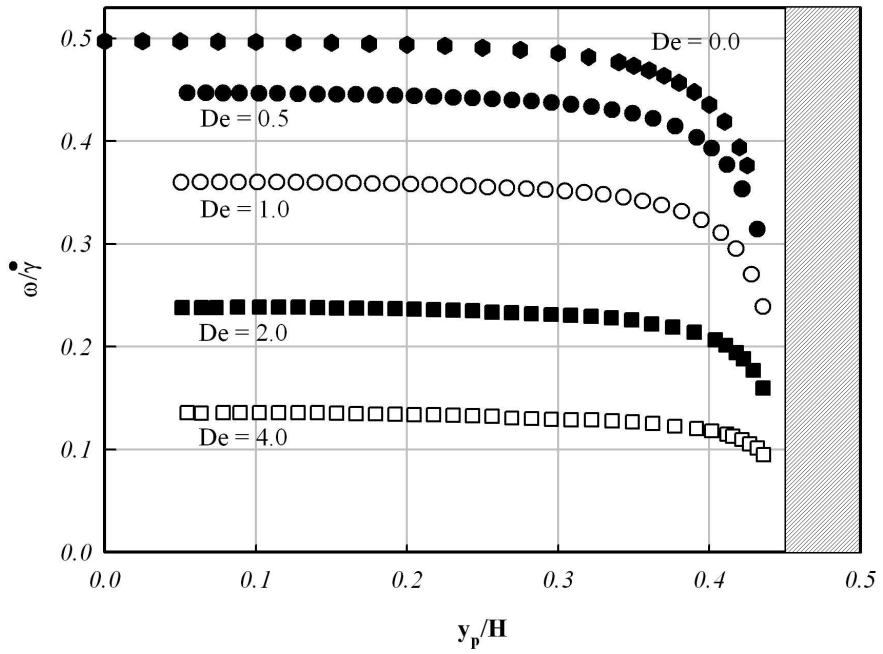

Figure 26: Particle angular velocities (ω) as a function of particle y-position (y_p) at different Deborah numbers (De). The other parameters are: $\alpha = 0.2$, $\eta_s/\eta_p = 0.1$, $D_p/H = 0.1$. The hexagons refer to the Newtonian case.

The effect of the Deborah number on the particle angular velocity is reported in figure 26 where ω as a function of the particle position is reported for different $De-$values (the Newtonian case is reported as well). A decreasing, monotonic trend is evident as De increases. The decreasing of ω with De is somehow similar to that observed by [43] for the case of a sphere with its center at the midplane of the shear cell.

Another interesting aspect is the effect of the shear thinning on the particle motion. The Giesekus model, Eq. (6), predicts the shear thinning phenomenon in shearing flows modulated by the parameter α: The thinning is more and more pronounced as α increases and, for $\alpha = 0$, the

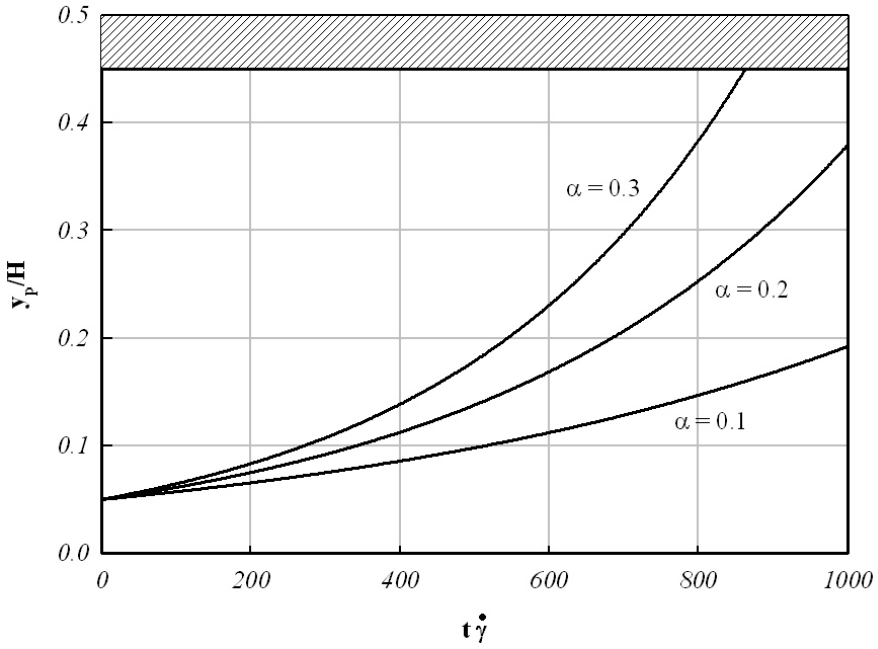

Figure 27: $y-$position of particle center (y_p) as a function of time (t) for different Giesekus constitutive parameter (α). The other parameters are: $De = 1.0$, $\eta_s/\eta_p = 0.1$, $D_p/H = 0.1$.

upper convected Maxwell model is recovered (no shear thinning). The influence of thinning on particle migration is then investigated by varying α. In figure 27 the particle trajectories for three different values of α are reported at fixed $De = 1$. By increasing α, the particle moves faster towards the wall, i.e. the migration velocity is higher. Thus, a particle suspended in a Maxwell fluid is expected to experience the slowest migration rate.

6.1.3 Particle translational $x-$velocity

We finally consider the last state variable in a 2D one-particle system, namely, the particle $x-$velocity, U_p. Indeed, due to the external imposed flow, the particle translates along the $x-$direction for both Newtonian and viscoelastic suspending fluid, with a velocity that is in general dif-

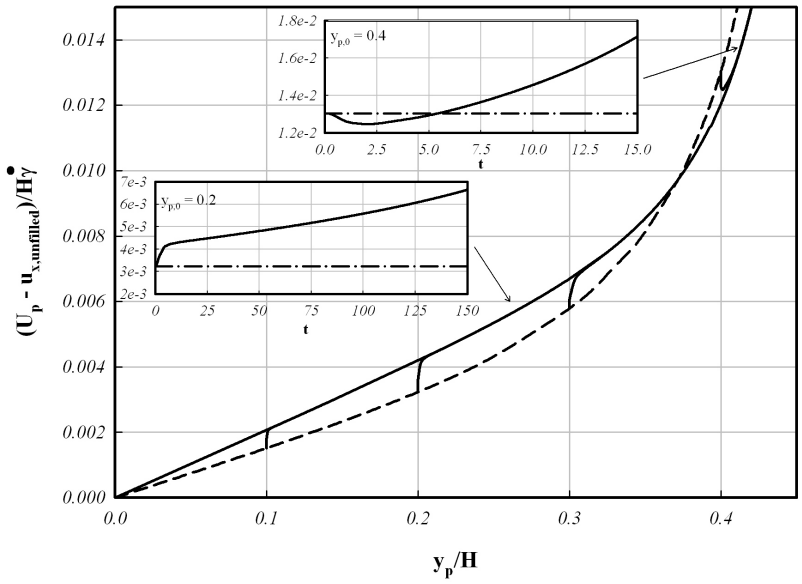

Figure 28: Particle slip velocity ($U_p - u_{x,unfilled}$) as a function of position (y_p) for different starting positions (solid lines). The other parameters are: $De = 2.0$, $\alpha = 0.2$, $\eta_s/\eta_p = 0.1$, $D_p/H = 0.1$. The dashed line refers to a Newtonian suspending fluid. In the insets $U_p - u_{x,unfilled}$ is reported as function of time for $y_{p,0} = 0.2$ and $y_{p,0} = 0.4$.

ferent from the one ($u_{x,\text{unfilled}} = \dot{\gamma} y$) experienced by the unfilled fluid at the same vertical position as the particle center.

In figure 28 the relative particle $x-$velocity, $U_p - u_{x,\text{unfilled}}$, usually termed the slip velocity, is reported as function of particle position for $D_p/H = 0.1$ for both the Newtonian and a Giesekus fluid with $De = 2.0$, $\alpha = 0.2$. In the whole channel, and for both fluids, the particle moves faster than the unfilled fluid, i.e., the particle 'leads' the fluid. For the Newtonian case, such a result was analytically demonstrated long ago [27,].

The dashed curve in figure 28 is the Newtonian prediction. Due to the absence of the migration phenomenon, a particle in a Newtonian fluid keeps its horizontal velocity during the motion. In other words,

the dashed curve only gives the locus of the translational velocities for different vertical positions. On the other hand, a particle in a viscoelastic fluid migrates while horizontally translating, hence its horizontal velocity changes in time: the solid line in figure 28 is travelled in time. As a matter of fact, an initial transient behaviorù

characterized by a fast change in U_p is found at start-up (the almost vertical lines departing from the Newtonian curve). The start-up is clearly visible in the inset where U_p versus time is reported for two different starting positions. The dash-dotted line is the Newtonian prediction that is of course constant in time. In the non-Newtonian case, after the extinction of the initial fast transients, the horizontal velocity reaches a master curve from whatever initial starting position. Even with this state variable, therefore, a slow dynamics is attained, similarly to what observed for the migration velocity. The viscoelastic curve in figure 28 is higher than the corresponding Newtonian one in a large central part of the channel, whereas the trend is inverted as the particle is close to the wall.

6.2 Migration of particle under oscillatory shear flow

In this section the results of 2D simulations of a particle moving under an oscillatory shear flow are presented. The aim of this set of simulations is to compare our results with the experimental data of Lormand and Phillips, so, as stated in Chapter 5, the height of the domain and the radius of the particle are chosen in order to respect the geometrical dimensions used in the experiments. The geometrical parameters are described in Chapter 5.2.2. As written above, the particle is subjected to a oscillatory shear flow, so we want to check, in particular, the effect of amplitude A and frequency f of the applied square wave. Such effects can be studied independently by varying the Deborah number De and the Strouhal number St. These two dimensionless numbers are defined as follow

$De{=}\lambda\dot{\gamma}$ and $St{=}f/\dot{\gamma}$

in which λ is the relaxation time of the suspending fluid. Notice that in their experiments Lormand and Phillips do not refer directly to De and St: they changed these two dimensionless numbers by varying the frequency and the amplitude of the square wave imposed. In the first experiment, they fixed the amplitude of the square wave and varied only the frequency. In order to do that, they changed also the velocity of the moving cylinder (the inner one) and, consequently, the shear rate so the Strouhal number was fixed. In the second experiment, they varied both the amplitude and the frequency of the square wave in order to fix the angular velocity of the moving cylinder, so they fixed the Deborah number.

In all the following simulations we do not change the suspending fluid, so we can vary De only by varying the shear rate $\dot{\gamma}$. On the contrary, we can change St by varying both the shear rate $\dot{\gamma}$ and the frequency f. The time step is fixed to $\Delta t = 0.015$

As shown in the previous chapter, a particle suspended in a viscoelastic fluid subjected to continuous shear flow migrates toward the wall. Our aim is to understand the effect of the oscillatory shear flow on the motion of the particle. Results show that, by oscillating the two plates, the migration velocity decreases. This is shown in figure 29 in which the particle position as a function of time is reported. All the curves are obtained for the same Deborah number. The solid line refers to a

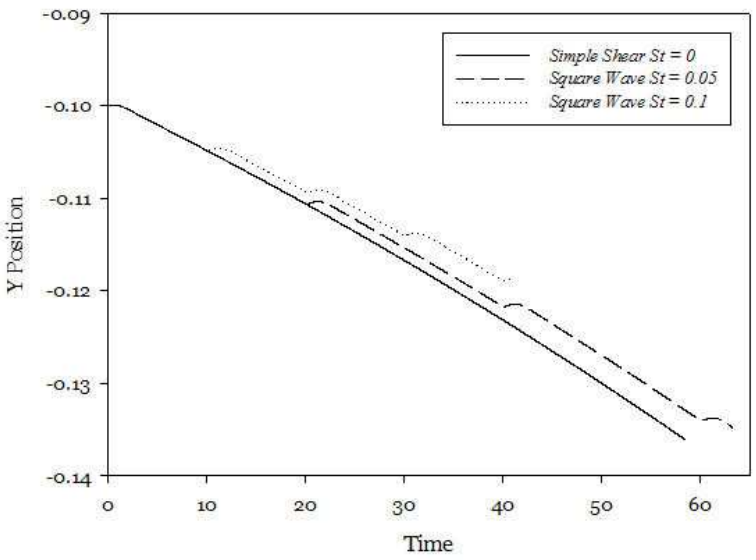

Figure 29: Particle $y-$position versus time. The effect of oscillation on particle migration. Different lines refers to different values of St. The other parameters are De=0.2, $\dot{\gamma}$=1,α=0.2

particle moving under simple shear flow ($St = 0$). We can notice that when the St number increases the particle moves slower. By observing the migration velocity of the particle as a function of the time (figure 30), we can observe an initial transient due to the development of viscoelastic stresses. Notice that initially the two curves are perfectly superimposed. When the plates invert their motion, we can notice a similar transient which correspond to a pause in the particle motion.

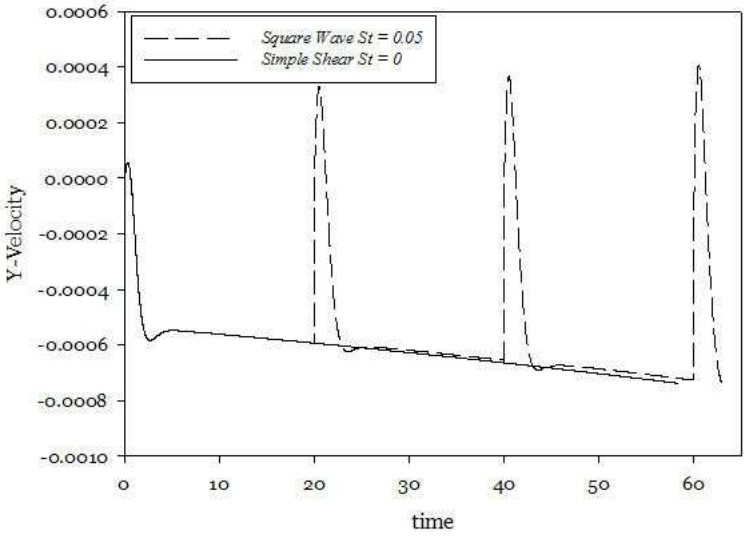

Figure 30: Particle $y-$velocity versus time. Transients in velocity for any inversion in the motion of the two plates

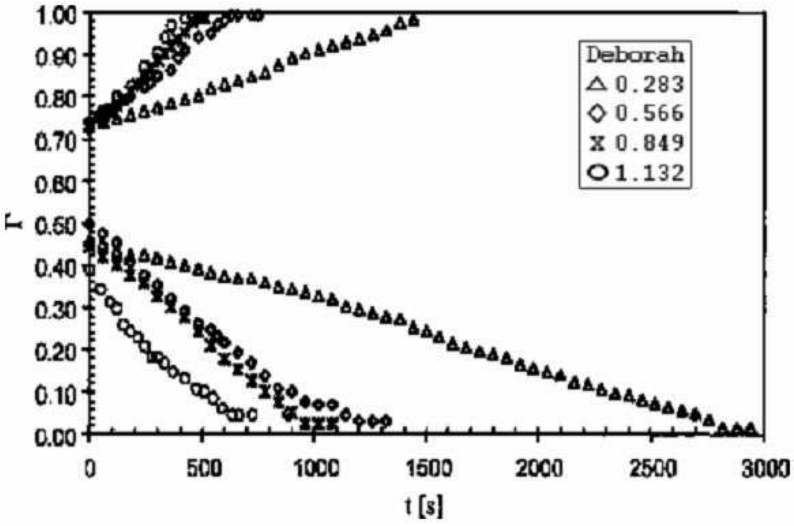

Figure 31: radial position of particle center (Γ) as a function of time (t). $\Gamma = 0$ refers to the outer cylinder, $\Gamma = 1$ refers to the inner cylinder.(from [29])

6.2.1 Effect of Deborah number

As written before Lormand and Phillips investigated the influence of frequency and amplitude of the square wave on the particle motion.

The first aspect we want to analyze is the behavior of the particle if we change only the Deborah number i.e. by varying both the frequency, f, and the shear rate, $\dot{\gamma}$, in order to maintain the Strouhal number constant.

The suspending fluid is a Giesekus fluid (α=0.2, λ=0.2).

In the figure 31 the results obtained by Lormand and Phillips are reported. They performed these experiments by changing the frequency of the square wave without varying its amplitude. They obtained that by increasing f the particle moves faster toward the closer plate. Notice that all the particles start at the same initial position. We changed the legend on the original picture of Lormand and Phillips for a better comparison with our result.

As written above we performed simulations at different Deborah numbers with a constant Strouhal number $St = 0.177$. In table 1 the values of shear rate $\dot{\gamma}$, frequency f and Deborah De are reported.

In figure 32 the results of our simulations are shown: we reported the

shear rate $\dot{\gamma}$	frequency f	Strouhal St	Deborah De
1.415	0.25	0.177	0.283
2.830	0.50	0.177	0.566
4.245	0.75	0.177	0.849
5.660	1.00	0.177	1.132

Table 4: Operating parameters used in simulations at different De

y-trajectories of the particles as function of time. We can report only half of the channel for symmetry.

Our results are in qualitative agreement with the ones of Lormand and Phillips. We can observe the same behavior in the motion of the particle: the migration rate is strongly affected by the frequency of the square wave imposed, in fact increasing f the particle reaches faster the wall.

The small "jumps" in the trajectories are due to the inversions in the motions of the plates as shown before in figure 29.

In the previous chapter, we showed the effect on Deborah on particle migration in continuous shear; we can confirm that also in an oscillatory shear flow, the effect of increasing De is to increase the particle migration rate.

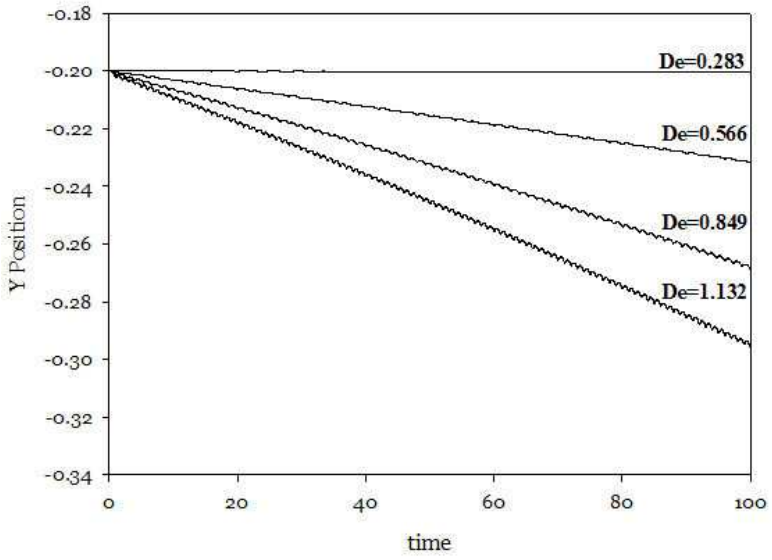

Figure 32: $y-$position of particle center as a function of time (t) for different values of De.

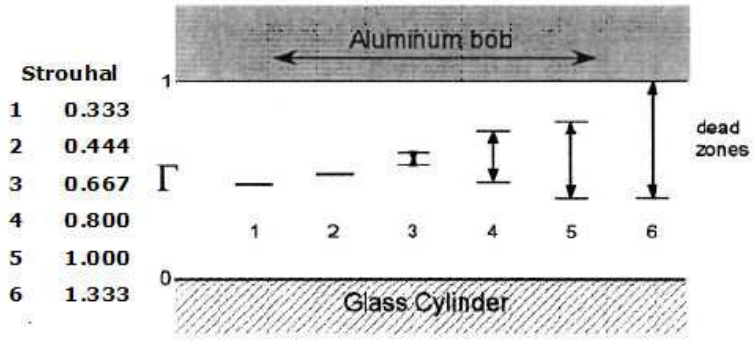

Figure 33: Dead zones for different values of St number.(from [29])

6.2.2 Effect of Strouhal number

The second aspect that we want to analyze is the effect of the amplitude of the square wave on the migration.

As written above, Lormand and Phillips studied the effect of the amplitude of the square wave by varying the frequency without changing the angular velocity of the rotating cylinder. In this way they changed only the Strouhal number without changing the Deborah number.

They found the presence of a "dead zone" (figure 33): if the initial position of the particle is in this region of the channel, they cannot observe radial migration. Also in this case we changed the legend in the Lormand and Phillips figure for better comparison with our result.

The presence of the dead zone is strictly related to the amplitude of the square wave: for large values of the amplitude, i.e. for small values of the St number, the dead zone reduced to a single line; by decreasing A,instead, i.e. by increasing St, the dead zone enlarge and only the particles closer to the wall can migrate.

In table 2 our working parameters are reported. We fixed De=0.6 and we varied the St number.

Also in this case we found a qualitative agreement with the experimental results. In figure 34 we report the particle y-positions as a function of time. We show only the result for particles starting at $y = 0.3$, but the behavior is the same for all the initial position. For small St

frequency f	Strouhal St
1.000	0.333
1.333	0.444
2.000	0.667
2.400	0.800
3.000	1.000
4.000	1.333

Table 5: Operating parameters used in simulations at different St

number, the particle migrates toward the closer plate from any initial position. Increasing St, the particle velocity decreases and for $St > 1$ number we in fact observe an inversion in the motion of the particle.

This inversion in the migration direction can be explained by considering the transient in the velocity. High values of St number correspond to high values of the frequency, i.e. to low values of the inversion time of the square wave.

The inversion in the trajectories are probably due to the fact that when the plates invert their motion, the velocity has not yet reached its stationary value. As shown in figure 30, we can notice transients in particle velocities for any inversion in the motion of the plates. During these transients, the sign of velocity inverts, so if the inversion occurs during the transient, the direction of migration can change.

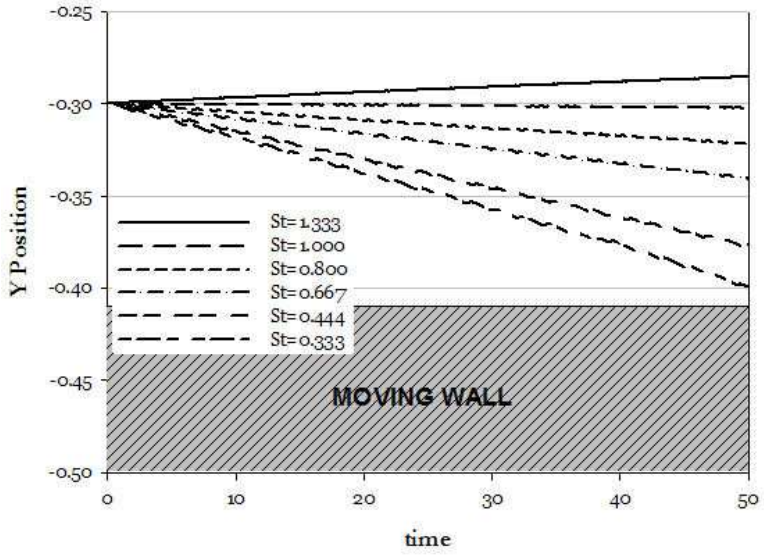

Figure 34: $y-$position of the particle as a function of time for different values of St.

6.3 Effect of curvature on the migration of particles

In this section the effect of curvature on particle migration is presented.

As shown by Lormand and Philips experiments, a particle subjected to shear flow between two concentric cylinders migrates in the radial direction toward one of the wall. As written in their work, they tried to minimize the effect of curvature by using very small particles. However, by observing the trajectories of the particle, (figure 35), we can notice that there is no symmetry in the channel: in fact, the particle with the initial position on the center line migrates toward the outer cylinder.

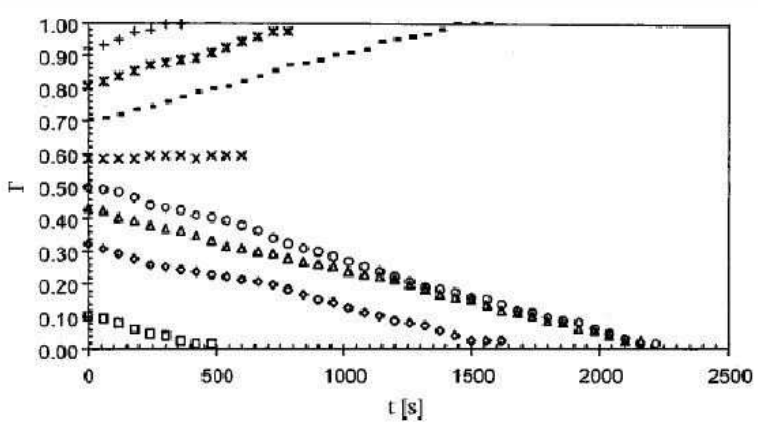

Figure 35: radial position of particle center (Γ) as a function of time (t). $\Gamma = 0$ refers to the outer cylinder, $\Gamma = 1$ refers to the inner cylinder.(from [29])

In order to investigate the migration of particle between two concentric cylinders, we performed numerical simulations in the 2D domain described in section 5.2.3.

In the same section, we checked the convergence in space and time for every situation investigated. The time step size is fixed to $\Delta t = 0.005$.

In figure 36 the radial position of the particle as a function of time is reported. The suspending fluid is a Giesekus fluid and the parameters chosen are: $De = 3.0$, $\alpha = 0.2$, $\eta_s/\eta_p = 0.1$ and $D_p/H = 0.1$, in which H is the gap between the two cylinders. Notice that we chose the radii of the cylinders, the gap and the particle radius in order to respect the operating parameters used by Lormand and Phillips in their experiments.

The radial position $y_p = -0,5$ refers to the outer cylinder (steady) and the radial position $y_p = 0,5$ refers to the inner cylinder, which is the moving one. Depending on the initial position, the particle moves toward the inner or the outer cylinder.

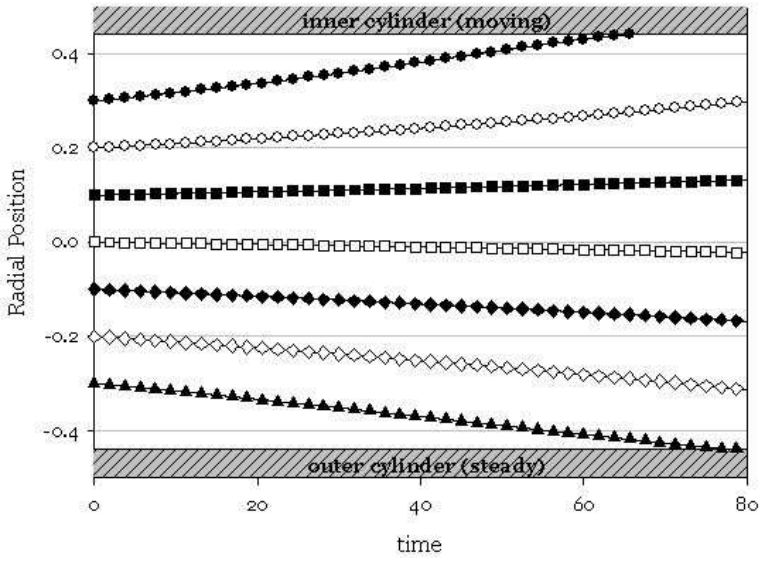

Figure 36: Radial position of particle center (y_p) as a function of time (t) for different starting positions ($y_{p,0}$). The other parameters are: $De = 3.0$, $\alpha = 0.2$, $\eta_s/\eta_p = 0.1$, $D_p/H = 0.12$. The shaded area is the channel region unaccessible to the particle due to its finite size.

The migration velocity depends on the initial position: particles moving toward the inner cylinder are faster than particles moving toward the outer. As showed in section 5, if we consider the radial velocity as a function of the radial position, we can notice that all the curve collapse onto a single curve. The migration velocity as a function of the radial position of the particle is reported in figure 37. The symbols are the same used in figure 36 and refer to the values of velocity calculated by simulations. These data can be fitted with a polynomial (black line in figure 37) with the following functional form:

$$V_p = m_0 + m_1\, y_p + m_2\, y_p^2 + m_3\, y_p^3 + m_4\, y_p^4 + m_5\, y_p^5 \qquad (46)$$

Notice that in these case the term m_0 is not zero, in fact there no simmetry in the channel.

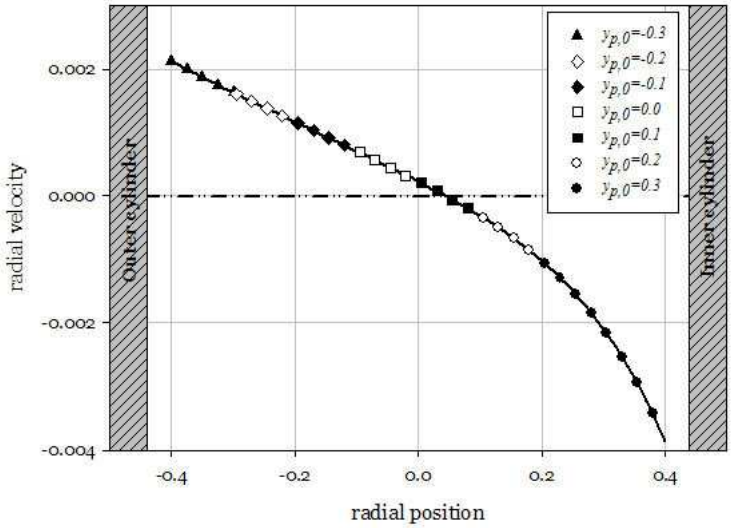

Figure 37: Particle migration velocities (V_p) as a function of particle radial positions. The other parameters are: $De = 3.0$, $\alpha = 0.2$, $\eta_s/\eta_p = 0.1$, $D_p/H = 0.12$. The black line is the function reported in Eq. (46). The shaded area is the channel region unaccessible to the particle due to its finite size.

By integrating numerically this functional form we can recover the particle trajectory in time over the channel with initial condition $t = 0 \Rightarrow y_p = y_{p,0}$.

In figure 38, the master curve is reported with a black line. The symbols refer to the curves calculated through numerical simulations reported in figure 36: different symbols refer to different starting initial positions. The overlap for any starting position $y_{p,0}$ confirms the validity of in the whole channel: in conclusion, each individual trajectory, just translated in time, is a part of an unique behavior.

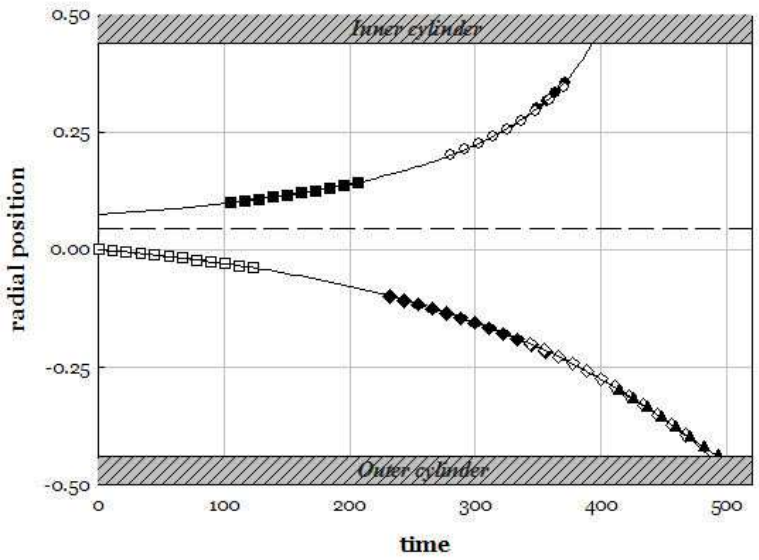

Figure 38: Master curve (black line) and the simulated trajectories reported in figure 36. The parameters are: $De = 3.0$, $\alpha = 0.2$, $\eta_s/\eta_p = 0.1$, $D_p/H = 0.12$. The shaded area is the channel region unaccessible to the particle due to its finite size.

We emphasize that also the particle starting on the channel centerline migrates toward the outer cylinder. The dashed line in figure 38 represents instead the position of zero migration velocity: a particle initially located with the center exactly at this position will only rotate. Notice that the distance between this line and the center line of the channel is very small because in this case the curvature is not so strong.

In order to understand the effect of curvature, we performed another series of simulations, changing the radii of the cylinders, but with the distance between the two cylinders as well as the particle radius kept fixed. All these simulations are performed with the same suspending fluid, so $De = 3.0$, $\alpha = 0.2$, $\eta_s/\eta_p = 0.1$. The different geometrical parameters are reported in table IV

In figure 39 the migration velocity as a function of the radial position of the particles is reported: different curves refer to different curvatures. The black squares refer to the particle moving between two

Inner radius R_i	Outer Radius R_e
20	21
10	11
5	6
1	2

Table 6: Geometrical parameters of the domain

parallel plates. The black lines are obtained by interpolating the points of every single curve with a polynomial Eq. (46), as done before.

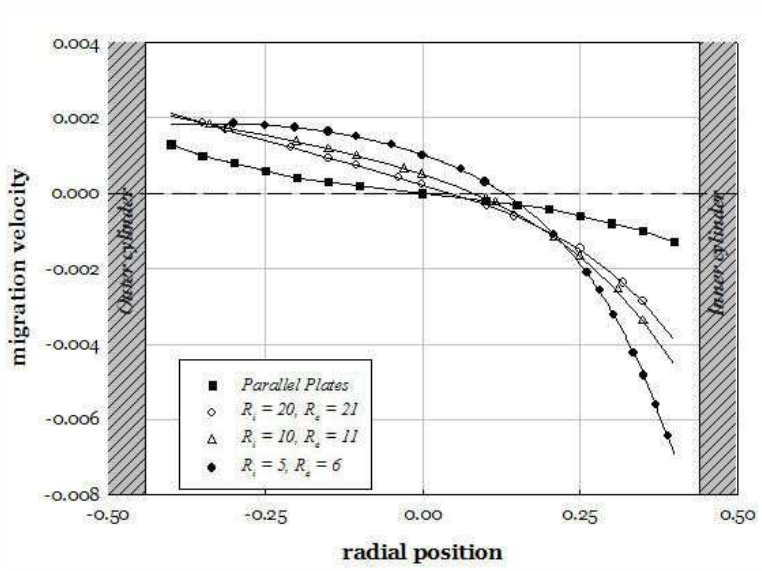

Figure 39: Particle migration velocities (V_p) as a function of particle radial positions. The other parameters are: $De = 3.0$, $\alpha = 0.2$, $\eta_s/\eta_p = 0.1$, $D_p/H = 0.12$. Different lines refers to different geometries. The shaded area is the channel region unaccessible to the particle due to its finite size.

The migration velocity is equal to zero exactly in the center line of the channel when a particle moves between two parallel plates. By increasing the curvature, the point of zero migration tends to move far from the centerline.

We can find master curves also for the other curvatures as reported in figure 40

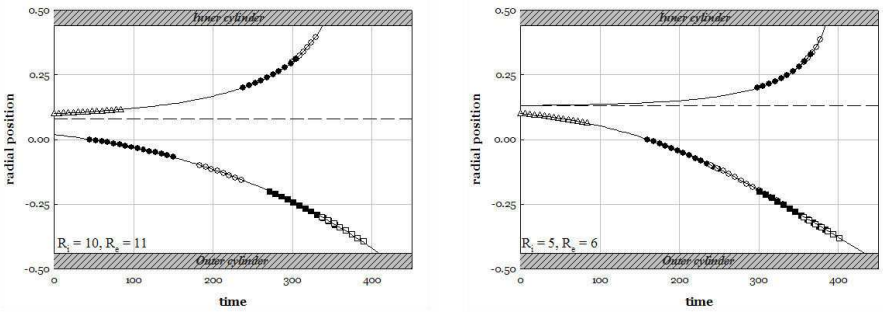

Figure 40: Master curve describing the particle migration. The parameters are: $De = 3.0$, $\alpha = 0.2$, $\eta_s/\eta_p = 0.1$, $D_p/H = 0.12$. The shaded area is the channel region unaccessible to the particle due to its finite size. The left figure refers to $R_i = 10$, the right picture to $R_e = 5$

Also in these two cases, there is a perfect overlap between the single trajectories shifted in time and the master curves.

We further increase the curvature to stress its effect on particle migration. In figure41 the master curve obtained in this extreme case is reported. We can notice that there is a difference in the convexity of the curve and that the point of zero velocity is more distant from the center line. We can also notice that particles starting near to the outer cylinder do not seem to reach the wall, but they can also move along it at fixed distance.

Finally, we report the position of the point of zero velocity as a function of the curvature defined as

$$Curvature = \frac{\ln R_e - \ln R_i}{R_e - R_i} \tag{47}$$

In the table 5 the values of curvature are reported

Curvature zero refers to the case of particle moving between two parallel plates, and the point of zero velocity is exactly in the center line. Increasing curvature, the point of zero velocity moves toward the inner cylinder. Probably, increasing furthermore the curvature, the point of zero velocity will reach a stationary value.

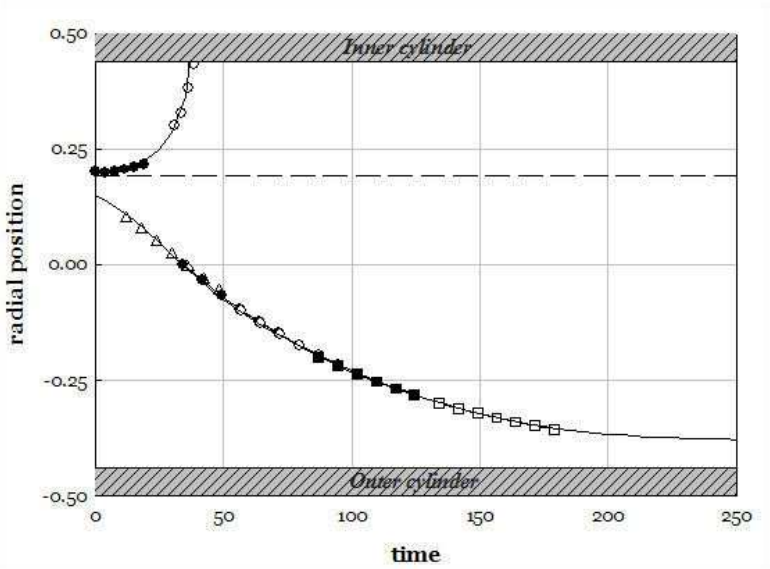

Figure 41: Master curve obtained for $R_e = 2$ and $R_i = 1$ (black line). The parameters are: $De = 3.0$, $\alpha = 0.2$, $\eta_s/\eta_p = 0.1$, $D_p/H = 0.12$. The shaded area is the channel region unaccessible to the particle due to its finite size.

Inner radius	Outer Radius	Curvature
20	21	0.048790
10	11	0.095310
5	6	0.182322
1	2	0.693147

Table 7: Values of curvature

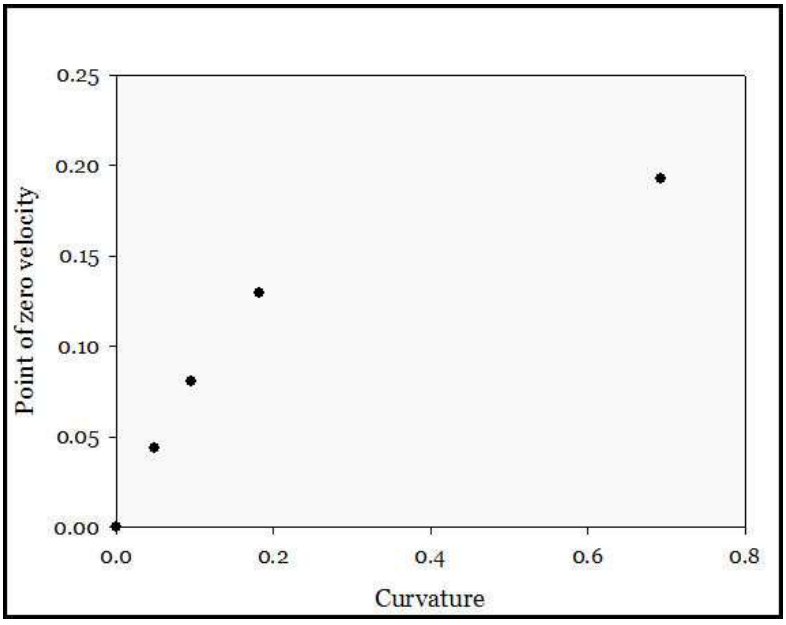

Figure 42: Point of zero velocity position as a function of the curvature defined as Eq. (47). The parameters are: $De = 3.0$, $\alpha = 0.2$, $\eta_s/\eta_p = 0.1$, $D_p/H = 0.12$.

6.3.1 Effect of suspending fluid

As stated in the previous section, the principal effect of curvature is to break the symmetry in the channel. We want also to investigate the effects of the suspending fluid on the migration. In order to do that, we change the parameters of the Giesekus fluid. In particular we want to study the effect of the mobility α and of the relaxation time λ, in particular changing α we change the shear thinning (α=0 means that the viscosity of the fluid is constant with the shear rate $\dot{\gamma}$).

The geometrical parameters used in this case are: $R_i = 5$, $R_e = 6$, $D_p = 0.12$. In figure 43 the particle radial position as a function of time is reported. The solid lines refer to a Giesekus fluid with $De = 3.0$, $\alpha = 0.2$ and are the same results presented in figure 36. The dashed curves refer to a Giesekus fluid with $De = 6.0$, $\alpha = 0.2$ and the dotted curve refer to a Giesekus fluid with $De = 3.0$, $\alpha = 0.4$. Increasing De and α the migration velocity increase.

Also in these cases we can find two master curves for the radial positions of the particle reported in figure 44.

In figure 45 the radial velocity of the particle versus time is reported. The point of zero velocity depends also on the suspending fluid: increasing De and α this point tends to move toward the center line.

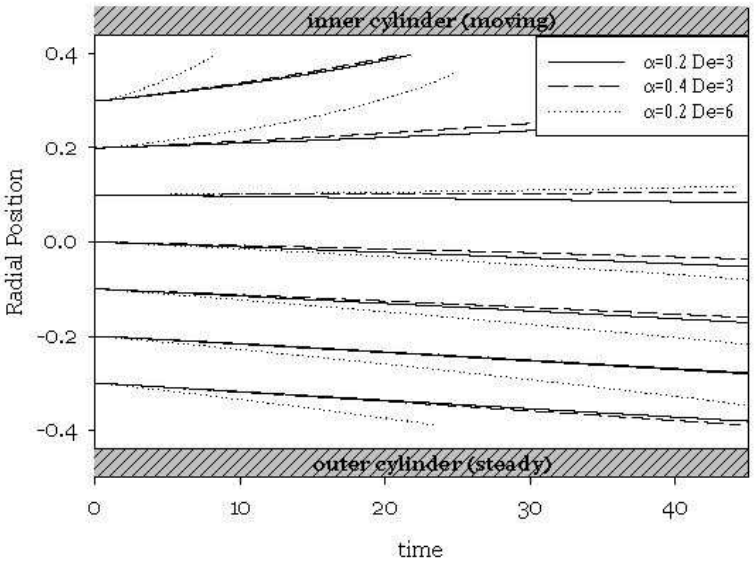

Figure 43: Radial position of particle center (y_p) as a function of time (t) for different starting positions ($y_{p,0}$). The geometrical parameters are $R_i = 5$, $R_e = 6$, $D_p = 0.12$. The black lines refers to a Giesekus fluid with $De = 3.0$ and $\alpha = 0.2$; the dashed line refers to a Giesekus fluid with $De = 6.0$ and $\alpha = 0.2$; the dotted line refers to a Giesekus fluid with $De = 3.0$ and $\alpha = 0.4$;

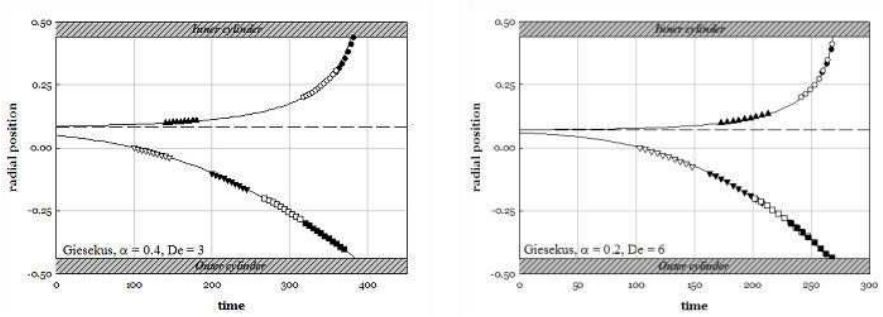

Figure 44: Master curves obtained with using different suspending fluids (black line). The left figure refers to $De = 3.0$ and $\alpha = 0.4$;, the right picture to $De = 6.0$ and $\alpha = 0.2$;

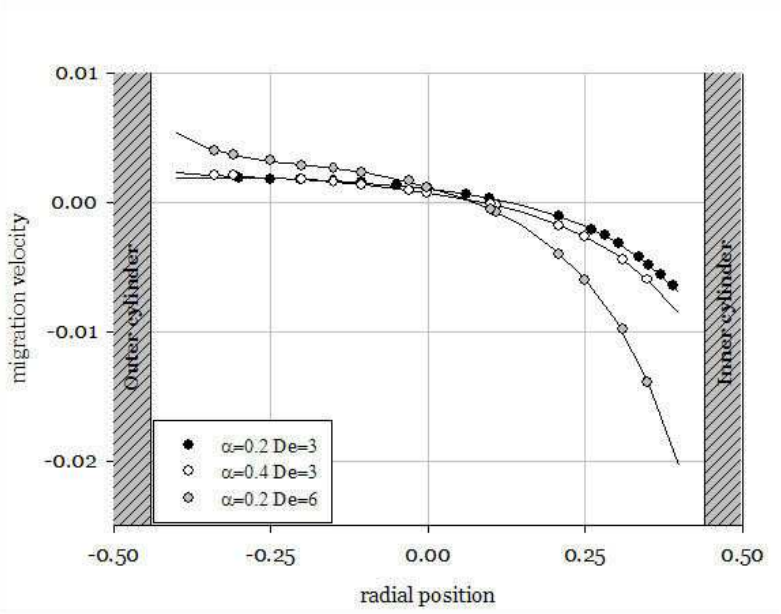

Figure 45: Particle migration velocities as a function of particle radial positions. The geometrical parameters are $R_i = 5$, $R_e = 6$, $D_p = 0.12$. Different lines refer to different suspending fluids.

6.3.2 Effect of particle size

Finally, we want to study the effect of particle size by varying the D_p/H ratio (dimensionless diameter. We fix $De = 3$ and $\alpha = 0.2$. Lormand and Phillips investigated the effect of particle size on the migration rate, but not on the point of zero velocity: they only showed that increasing the particle diameter the migration rate increases. This result is in perfect agreement with our simulation showed in Chapter 6.1.1.

Our aim is to investigate the effect of particle size on the point of zero velocity. In particular we double the particle diameter with respect to previous simulations to perform this set of simulations. We use the geometry with $R_i = 5$ and $R_e = 6$. Also in this case we can find a master curve, reported in figure 46

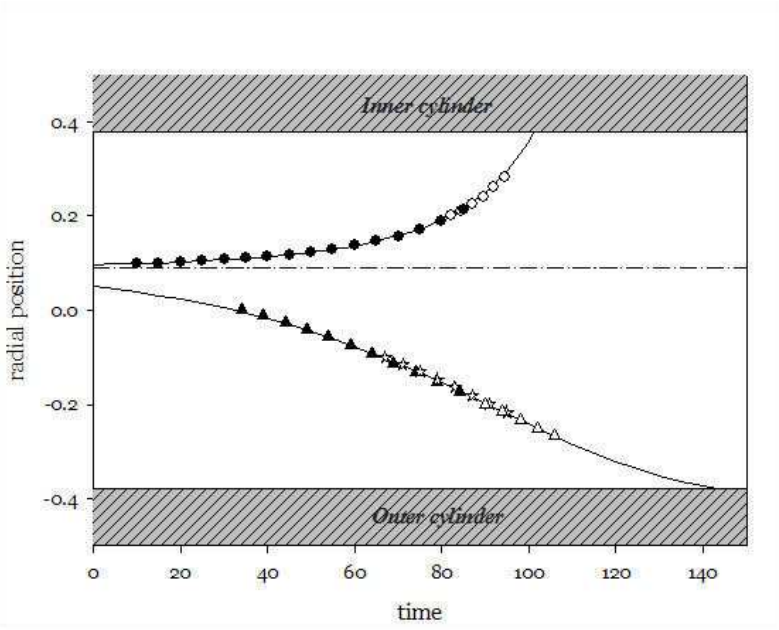

Figure 46: Master curve describing the particle migration. The parameters are: $De = 3.0$, $\alpha = 0.2$, $\eta_s/\eta_p = 0.1$, $D_p/H = 0.24$. The shaded area is the channel region unaccessible to the particle due to its finite size.

The point of zero velocity is at y=0.090, while with a smaller particle (see figure 40(b) the point of zero velocity is at y=0.130: increasing the particle diameter the position of the point of zero velocity tends to move

toward the center line. We expect that by increasing furthermore the particle size, the point of zero velocity will coincide with the center line of the channel: in this case the particle will only rotate as in the case of confined flow, but this still need to be tested.

7 Conclusions

In this thesis we study the motion of a 2D single, solid particle suspended in a viscoelastic fluid. We perform simulations by means of a finite elements method method. An ALE particle mover is combined with a DEVSS-G/SUPG formulation together with a log-representation of the conformation tensor, in order to easily manage the particle motion and significantly improve numerical convergence at finite Deborah numbers. Finally, the rigid-body motion on the particle boundary is imposed through Lagrange multipliers.

In Chapter 6.1 we study the motion of a single particle under continuous shear flow. The suspending fluid is a Giesekus fluid, i.e. a shear thinning fluid in which both the first and second normal stresses difference are present. The result of this set of simulation is that the particle migrates toward the wall from any initial position with the exception of the particle starting exactly in the midline of the channel, which, due to the symmetry, can only rotate. The main finding of this work is that, for a given set of geometrical and fluid parameters, the migration velocity behavior in the whole channel can be described by a single curve. As a consequence, regardless the starting position (and after extinction of the initial transients due to the development of stresses), the particle trajectories collapse on a master curve. The we analyze the effect of particle size on the migration: we find that the migration rate increases with the particle size, in perfect qualitative agreement with the results of Lormand and Phillips [29]. We also study the effect of the suspending fluid on the motion of the particle. The results show that the particle moves faster toward the wall if we increase the α in the Giesekus equation (Eq. (6)), i.e. in a fluid in which the shear thinning is more pronounced.

In Chapter 6.2 we analyze the motion on the particle under oscillatory shear flow. We apply a square wave on the moving plates, which is characterize by two parameters: the amplitude A and the frequency f. Amplitude and frequency are varied so that we can simulate under the same operative conditions used by Lormand and Phillips[29] in their experiments. As explained in section changing these parameter is equivalent to vary the Strouhal number, St, and the Deborah number, Des. We perform two sets of simulations. In the first one we change De at a fixed St. We notice that increasing De we increase the migration rate of

the particle. In the second set of simulation we vary the St at a fixed De. Notice that $St = 0$ is the case of continuous shear flow. Increasing St the particle moves slower toward the wall, and for high values of St ($St > 1$) the particle migrates in the opposite direction. The inversion in migration is due to the fact that the time of inversion of the square wave is less than the time of the completely development of normal stress.

In Chapter 6.3 we show the effect of curvature on the migration. Lormand and Phillips([29]) results (see Fig. 35) show that there is no symmetry in the trajectories during migration. Our data show the same trend of the experiments. We notice that also for low values of curvature, we do not have symmetry in the channel: also the particle starting in the midline of the channel migrates toward the wall. Increasing furthermore the curvature, the point of zero velocity tends to move toward the inner cylinder. The important results is that also in this case we find master curves for trajectories. All the master curves show the same trends with the exception of the curve obtained for every strong curvature (see Fig.41): a particle starting near the outer cylinder can not reach the wall. Finally, we investigate the effect of suspending fluid and particle size on the point of zero velocity.

References

[1] A. Einstein. Berichtigung zu Meiner Arbeiten: Eine Neue Bestimmung der Molekul Dimensionen. *Annalen der Physik Berlin*, 19:289, 1906.

[2] H. Brenner. Suspension rheology. *Proc. Heat and Mass Transfer*, 89:5, 1972.

[3] D.R. Foss and J.F. Brady. Structure, diffusion and rheology of brownian suspensions by stokesian dynamics simulation. *J. Fluid Mech.*, 167:407, 2000.

[4] C.J. Petrie. The rheology of fibre suspensions. *J. Non-Newtonian Fluid Mech.*, 87:369, 1999.

[5] H.M. Laun. Rheological properties of aqueous polymer dispersions. *Angew. Makromol.Chem.*, 335:124–125, 1984.

[6] S. Taneda. Experimental investigation of the wake behind a sphere at low reynolds numbers. *J. Phys. Soc. Jpn*, 11:1004, 1956.

[7] S. Taneda. Visualization of separating stokes flows. *J. Phys. Soc. Jpn*, 46:1935, 1979.

[8] G. Segré and A. Silberberg. Radial particle displacemente in poiseuille flow suspensions. *Nature*, 189:209–210, 1961.

[9] G. Segre and A. Silberberg. Behaviour of macroscopic rigid spheres in poiseuille flow. Part 2. Experimental results and interpretation. *J. Fluid Mech.*, 14:136–157, 1962.

[10] P. G. Saffman. The lift on a small sphere in a slow shear flow. *J. Fluid Mech.*, 22:385–400, 1966.

[11] E. S. Asmolov. Dynamics of a spherical particle in a laminar boundary layer. *Fluid Dyn.*, 25:886–890, 1990.

[12] J. B. McLaughlin. Inertial migration of a small sphere in linear shear flows. *J. Fluid Mech.*, 224:261–274, 1991.

[13] D. T. Leighton and A. Acrivos. The lift on a small sphere touching a plane in the presence of a simple shear flow. *Z. angew. Math. Phys.*, 36:174–178, 1985.

[14] P. Cherukat and J. B. McLaughlin. The inertial lift on a rigid sphere in a linear shear flow field near a flat wall. *J. Fluid Mech.*, 263:1–18, 1994.

[15] G. P. Krishnan and D. T. Leighton. Inertial lift on a moving sphere in contact with a plane wall in a shear flow. *Phys. Fluid*, 7:2538–2545, 1995.

[16] A. Karnis and S.G. Mason. Particle motion in sheared suspensions. xix. viscoelastic media. *T. Soc. Rheol.*, 10:571–592, 1966.

[17] F. Gauthier, H.L. Goldsmith, and S.G. Mason. Particle motions in non-newtonian media. i: Couette flow. *Rheol. Acta*, 10:344–364, 1971.

[18] T.E. Karis, D.C. Prieve, and S.L. Rosen. Anomalous lateral migration of a rigid sphere in torsional flow of a viscoelastic fluid. *J. Rheol.*, 28:381–392, 1984.

[19] T.E. Karis, D.C. Prieve, and S.L. Rosen. Lateral migration of a rigid sphere in torsional flow of a viscoelastic fluid. *AIChE J.*, 30:631–636, 1984.

[20] D. C. Prieve, M. S. Jhon, and T. L. Koenig. Anomalous migration of a rigid sphere in torsional flow of a viscoelastic fluid. ii. effect on shear rate. *J. Rheol.*, 29:639–654, 1985.

[21] J. Feng and D.D. Joseph. The motion of solid particles suspended in viscoelastic liquids under torsional shear. *J. Fluid Mech.*, 324:199–222, 1996.

[22] J. Michele, R. Patzold, and R. Donis. Alignment and aggregation effects in suspensions of spheres in non- newtonian media. *Rheol. Acta*, 16:317–321, 1977.

[23] M. A. Jefri and A. H. Zahed. Elastic and viscous effects on particle migration in plane-poiseuille flow. *J. Rheol.*, 45:881–890, 1989.

[24] M. A. Tehrani. An experimental study of particle migration in pipe flow of viscoelastic fluids. *J. Rheol.*, 40:1057–1077, 1996.

[25] J. F. Morris and F. Boulay. Curvilinear flows of noncolloidal suspensions: The role of normal stresses. *J. Rheol.*, 43:1213–1237, 1999.

[26] A. Ponche and D. Dupuis. On instabilities and migration phenomena in cone and plate geometry. *J. Non-Newtonian Fluid Mech.*, 127:123–129, 2005.

[27] B.P. Ho and L.G. Leal. Migration of rigid spheres in two-dimensional unidirectional shear flow of a second-order fluid. *J. Fluid Mech.*, 76:783–799, 1976.

[28] P.Y. Huang, J. Feng, H.H. Hu, and D.D. Joseph. Direct simulation of the motion of solid particles in couette and poiseuille flows of viscoelastic fluids. *J. Fluid Mech.*, 343:73–94, 1997.

[29] B.M. Lormand and R.J. Phillips. Sphere migration in oscillatory Couette flow of a viscoelastic fluid. *J. Rheol.*, 48:551–570, 2004.

[30] R. Fattal and R. Kupferman. Constitutive laws for the matrix-logarithm of the conformation tensor. *J. Non-Newtonian Fluid Mech.*, 123:281–285, 2004.

[31] M. A. Hulsen, R. Fattal, and R. Kupferman. Flow of viscoelastic fluids past a cylinder at high weissenberg number: Stabilized simulations using matrix logarithms. *J. Non-Newtonian Fluid Mech.*, 127:27–39, 2005.

[32] R. Guenette and M. Fortin. A new mixed finite element method for computing viscoelastic flows. *J. Non-Newtonian Fluid Mech.*, 60:27–52, 1995.

[33] A. C. B. Bogaerds, A. M. Grillet, G. W. M. Peters, and F. P. T. Baaijens. Stability analysis of polymer shear flows using the extended pom-pom constitutive equations. *J. Non-Newtonian Fluid Mech.*, 108:187–208, 2002.

[34] A. N. Brooks and T. J. R. Hughes. Streamline upwind/Petrov-Galerkin formulations for convection dominated flows with particular emphasis on the incompressible Navier-Stokes equations. *Comput. Methods Appl. Mech. Eng.*, 32:199–259, 1982.

[35] G. D'Avino, P. L. Maffettone, M. A. Hulsen, and G. W. M. Peters. Numerical simulation of planar elongational flow of concentrated rigid particle suspensions in a viscoelastic fluid. *J. Non-Newtonian Fluid Mech.*, 150:65–79, 2007.

[36] H. H. Hu, N. A. Patankar, and M. Y. Zhu. Direct numerical simulations of fluid-solid systems using the Arbitrary Lagrangian-Eulerian technique. *J. Comp. Phys.*, 169:427–462, 2001.

[37] O. Schenk and K. Gartner. Solving unsymmetric sparse systems of linear equations with PARDISO. *Future Gener. Comput. Syst.*, 20:475–487, 2004.

[38] R. Glowinski, T.-W. Pan, D. D. Joseph, and T. I. Hesla. A distributed lagrangian multipliers/fictitious domain method for particulate flows. *Int. J. Multiphase Flow*, 25:755, 1999.

[39] W. R. Hwang, M. A. Hulsen, and H. E. H. Meijer. Direct simulation of particle suspensions in sliding bi-periodic frames. *J. Comp. Phys.*, 194:742, 2004.

[40] G. D'Avino, P. L. Maffettone, M. A. Hulsen, and G. W. M. Peters. A numerical method for simulating concentrated rigid particle suspensions in an elongational flow using a fixed grid. *J. Comp. Phys.*, 226:688–711, 2007.

[41] G. D'Avino and M. A. Hulsen. A comparison between a collocation and weak implementation of the rigid-body motion constraint on a particle surface. *Int. J. Numer. Methods Fluids, under review*, 2009.

[42] G. D'Avino, M. A. Hulsen, F. Snijkers, J. Vermant, F. Greco, and P. L. Maffettone. Rotation of a sphere in a viscoelastic liquid subjected to shear flow. Part I: Simulation results. *J. Rheol.*, 52:1331–1346, 2008.

[43] G. D'Avino, G. Cicale, M. A. Hulsen, F. Greco, and P. L. Maffettone. Effects of confinement on the motion of a single sphere in a sheared viscoelastic liquid. *J. Non-Newtonian Fluid Mech.*, 157:101–107, 2009.

[44] M. T. Sullivan, K. Moore, and H. A. Stone. Transverse instability of bubbles in viscoelastic channel flows. *Phys. Rev. Lett.*, 101:244503, 2008.